SUPPLEMENTARY INFORMATION

A 2D copper-imidazolate framework without thermal treatment as an efficient ORR electrocatalyst for Zn–air batteries

Ana Franco,[a,#] José Ángel Salatti-Dorado,[b,#] Valentin García-Caballero,[b] Sebastián Lorca,[c] Luis Camacho,[b] Manuel Cano,[*b] Antonio J. Fernández-Romero,[c] Juan J. Delgado,[d] Juan J. Giner-Casares,[b] and Carolina Carrillo-Carrión[*e,f]

[a] Department of Organic Chemistry, University of Córdoba, Campus Universitario de Rabanales, E-14014, Córdoba, Spain.
[b] Department of Physical Chemistry and Applied Thermodynamics, Institute of Fine Chemistry and Nanochemistry (IUNAN), University of Córdoba, Campus Universitario de Rabanales, E-14014 Córdoba, Spain. M.C. co-corresponding author, *E-mail*: q82calum@uco.es
[c] Grupo de Materiales Avanzados para la Producción y Almacenamiento de Energía, Universidad Politécnica de Cartagena. Aulario II, Campus de Alfonso XIII, 30203 Cartagena, Spain.
[d] Departamento de Ciencia de los Materiales e Ingeniería Metalúrgica y Química Inorgánica, Universidad de Cádiz, 11510 Puerto Real, Cádiz, Spain.
[e] Institute for Chemical Research (IIQ), CSIC-University of Seville, Avda. Américo Vespucio 49, 41092 Sevilla, Spain. C. C.-C. corresponding author, *E-mail*: carolina.carrillo@csic.es
[f] Department of Organic Chemistry, University of Seville, C/ Professor García González 1, 41012 Sevilla, Spain.

TABLE OF CONTENTS

I. General information

Chemicals. All chemicals were purchased from Sigma Aldrich Chemical Co. and used as received.

Transmission Electron Microscopy (TEM). TEM analysis was performed to investigate the morphology of the 2DCIFs nanoparticles. TEM images were acquired using a JEOL TEM 1400 operated at 200 kV. Samples were prepared by drying, under ambient conditions, a diluted dispersion of the particles on 200 mesh copper grids coated with Formvar/carbon film. TEM-EDX analysis was carried out in a JEOL 2100Plus TEM with integrated Oxford INCA EDX system. For EDX, the sample was collected on a nickel TEM grid covered with a carbon film.

Scanning Electron Microscopy (SEM). SEM analysis was carried out to investigate the morphology and elemental composition of 2DCIFs nanoparticles. The analysis was performed in a JEOL JSM 7800F scanning electron microscope in backscattered electron mode at 3 kV. Samples were prepared by drying, under ambient conditions, a diluted dispersion of the particles on a silicon wafer substrate.

High-Resolution High-Angle Annular Dark Field Scanning Transmission Electron Microscopy (HR HAADF-STEM). This was performed on a FEI Titan Themis 60–300 Double Aberration Corrected microscope operated at 200kV. In order to obtain single atom resolution in HAADF-STEM mode, the aberrations of the condenser lenses were corrected up to fourth–order using the Zemlin tableau. In order to minimize the damage of the sample by the electron beam, a beam current of 20 pA, and a short dwell time (1ms) were used. The elemental maps by EDS technique were obtained using the high-efficiency SuperX G2 detection system integrated in the microscope.

Dynamic Light Scattering (DLS) and Zeta-Potential (ζ). Measurements were performed using a Malvern Zetasizer Nano ZSP equipped with a 10 mW He–Ne laser operating at a wavelength of 633 nm and fixed scattering angle of 173˚. For DLS analysis, diluted samples were loaded into a quartz cuvette and then three measurements, each consisting of twelve data runs, were taken at room temperature (25°C) after an equilibration step of 120 sec. The zeta-potential of the nanosheets dispersed in MilliQ water was measured with laser Doppler anemometry (LDA) by using the same Malvern Zetasizer Nano ZSP instrument.

Powder X-Ray Diffraction (PXRD). X-ray analysis of the crystalline powder of samples was performed using a Bruker D8-Advance Diffractometer. X-ray radiation of Cu Kα was used and the measurement range was from 5° and 70° (2θ) with a step of 0.02° (2θ).

X-Ray Photoelectron Analysis (XPS). A Physical Electronics PHI 5700 spectrometer (non-monochromatic Mg-Kα radiation, 300 W, 15 kV and 1253.6 eV) was used for XPS analysis. Spectra were recorded in the constant pass energy mode at 29.35 eV, using a 720 µm diameter analysis area. Charge referencing was carried out using the adventitious carbon peak (C 1s at 284.8 eV). The energy scale was calibrated using Cu 2p3/2, Ag 3d5/2, and Au 4f7/2 lines at 932.7, 368.2 and 84.0 eV, respectively.

Fourier-Transform Infrared Spectroscopy (FTIR). FTIR analysis was performed on a Bruker Tensor 27 spectrophotometer; spectra were recorded at room temperature in the range

between 400 and 4000 cm^{-1} with a resolution of 4 cm^{-1}. Dried samples were prepared on a KBr pellet under a pressure of 0.01 torr.

N_2 physisorption analysis. N_2 sorption isotherms (77 K) of powder samples were done in an Autosorb-iQ-2 MP/XR (Quantachrome). Before the measurement, the sample was evacuated at 150 °C for 16 h. The specific surface areas were calculated from the Barrett–Emmett–Teller (BET) method in the pressure interval P/P_o =0.01-0.3 (being P_o the saturation pressure). Pore volume and external surface area were calculated by the t-plot method. Pore size distributions were calculated from the desorption branch of the isotherm using the Barrett–Joyner–Halenda (BJH) method.

Thermogravimetric analysis (TGA). TGA of powder samples was performed using a Thermal Advantage SDT-600 instrument with a general heating profile from 30 to 600 °C and using a heating rate of 5 °C·min^{-1} under air in a flow of 100 mL·min^{-1}.

Electrocatalytic measurements. Electrochemical analysis of 2DCIF electrocatalyst materials were performed using a Potentiosat/Galvanostat (EmStat3, PalmSens) in a traditional three-electrode configuration. Rotating Disk Electrode (RDE) experiments were carried out using a Pine MSR rotator (Model AFMSRCE). A glassy carbon (GC) disk of 5 mm in diameter (Pine Instruments Company) was used as the working electrode, whilst an Ag/AgCl and graphite sheet electrodes were used as reference and counter electrodes, respectively. GC electrode was modified with the different synthesized 2DCIFs samples by simple drop-casting. For this, 25 µL of the sample dispersed in methanol (2 mg·mL^{-1}) was casted into the clean surface of the GC and dried overnight at 4°C. A Pt/C sample (10 wt% Pt) was prepared in a similar manner (i.e. without Nafion). CV measurements were recorded in N_2- and O_2-saturated 0.1 M KOH aqueous solutions as electrolytes. Current densities were calculated considering the geometric surface area of the GC electrode. Potentials measured using Ag/AgCl (3 M KCl) as reference electrode were normalized according to the reversible hydrogen electrode (RHE) through the Nernst equation.[1] The potential range used for the measurements was from 0.00 to -0.2 V (vs. RHE), while a scan rate of 10 mV·s^{-1} was employed both under static and dynamic conditions. In the latter case, rotation rates from 250 to 2500 rpm were applied. Koutecky-Levich (K-L) equations model was used to estimate the numbers of electrons transferred (n-values) per O_2 molecules, and additional kinetics parameters at 0.00 V (vs RHE).[2]

II. Synthesis of 2D Copper-Imidazolate Framework Nanosheets (2DCIFs)

II.1. Optimized synthetic procedure. The synthesis was carried following an optimized protocol developed by our group. The chemicals used for the synthesis are the following: imidazole-2-carboxaldehyde (ICA; Sigma Aldrich #272000), copper(II) chloride ($CuCl_2$; Sigma Aldrich #451665), and cetyltrimethylammonium bromide (CTAB; Sigma Aldrich #H5882). To optimize the reaction conditions, we performed a systematic experimental study of the following parameters: molar ICA/Cu ratio, CTAB concentration, and reaction time. The optimal values were fixed in order to achieve homogeneous nanosheets (in shape and size) and maximize the reaction yield. Briefly, an aqueous solution of $CuCl_2$ (4 mL, 25 mM) was added to an aqueous solution of ICA (4 mL, 50 mM) under magnetic stirring (350 rpm) at room temperature (RT). Immediately after a CTAB solution (4 mL, 0.25 mM) was added, the mixture was stirred for 5 min and left then undisturbed overnight (15 h) at RT. Note that to prepare the aqueous solution of ICA, this was heated in a water bath at 80 ºC until complete dissolution of ICA and left then to cool down to RT before use. The appearance of purplish turbidity was gradually observed during the formation of the 2DCIFs particles. Next day, the particles (purple crystals) were collected by centrifugation (10000 RCF, 5 min) and washed three times with methanol in order to remove the remaining water solvent and CTAB molecules. They were finally vacuum-drying and redispersed in methanol at a concentration of 2 $mg{\cdot}mL^{-1}$. This stock methanolic solution of 2DCIFs nanoparticles was stored in the fridge until use.

II.2. Influence of the copper precursor and solvent. The change of imidazole-2-carboxaldehyde (ICA) by 2-methylimidazole (MeImz) as organic linker did not lead to the formation of particles/crystals as it was indicated visually by the non-appearance of turbidity in the reaction mixture and also confirmed by SEM (Fig. S1). On the other hand, the formation of the nanosheets was observed when using water as solvent but not in methanol. When all the precursor solutions were prepared in methanol and mixed by following the described method, after 15 h of incubation the reaction media remained transparent (*i.e.,* non-turbid solution; bluish color coming from the dissolved Cu^{+2} ions), which rules out the nucleation and crystal formation. Furthermore, different copper precursors were used in order to investigate their effect in the nanoparticles' synthesis (Fig. S2). It is worth noting that while using $CuCl_2$ and $Cu(NO_3)_2$ as Cu(II) salts produced sheets particles, $Cu(OAc)_2$ did not; the non-appearance of turbidity with time in the latter case indicated the absence of MOF formation. This finding is not surprising since the large influence of the metal source in the MOF formation process (mainly in the nucleation stage) has already been reported for other MOFs.

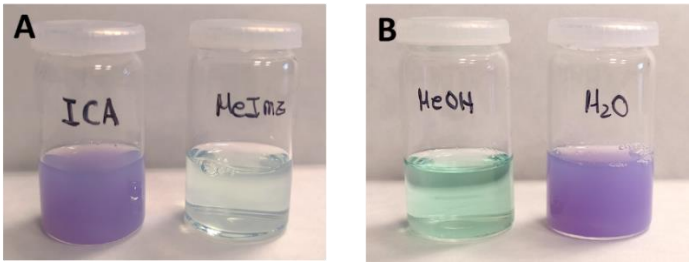

Fig. S1. Photographs of the syntheses under different conditions: (A) Variation of the imidazole ligand used (ICA or MeImz), and (B) Change of the reaction media (water or methanol) under optimized procedure described above.

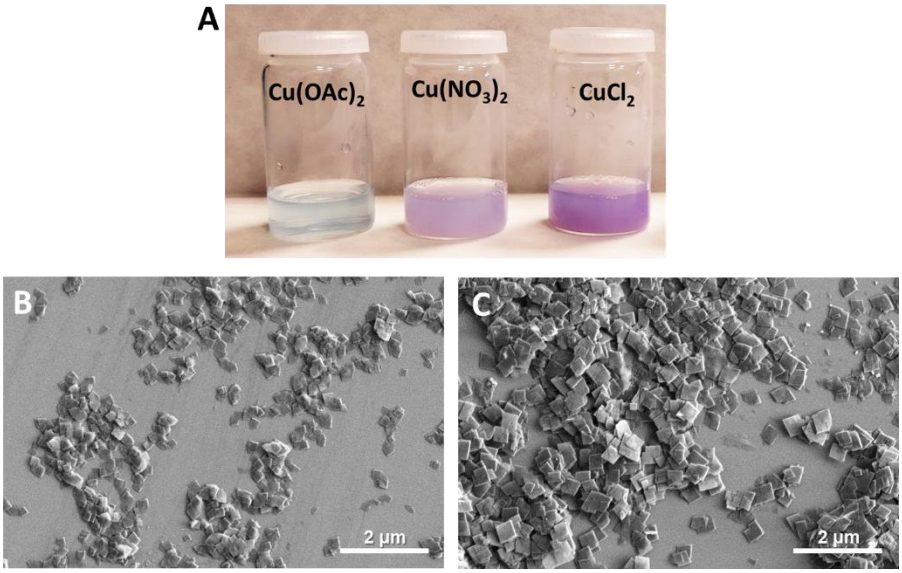

Fig. S2. Syntheses from different copper precursors: (A) Photographs of the mixture solutions after reaction (15 h) of the samples obtained by using different copper salts as precursors. Note that $Cu(OAc)_2$ did not result in turbidity after the incubation/reaction time, indicating the absence of particle formation (as also confirmed by SEM); (B) SEM image of 2DCIFs nanosheets obtained with $Cu(NO_3)_2$; (C) SEM image of 2DCIFs nanosheets obtained with $CuCl_2$.

II.3. Scale-up synthesis. Upscaling trials were done by increasing the volumes of precursor solutions. An 10x up-scale (*i.e.,* synthesis final volume from 10 mL to 100 mL) did not affect the quality of the obtained 2DCIFs particles (Fig. S3), and it was then used for further structural analysis. Larger scaling-up (30x), however, decreased slightly the crystallinity of the particles and also decreased the homogeneity of the particle sizes (as determined by SEM images and a higher polydispersity index in DLS measurements).

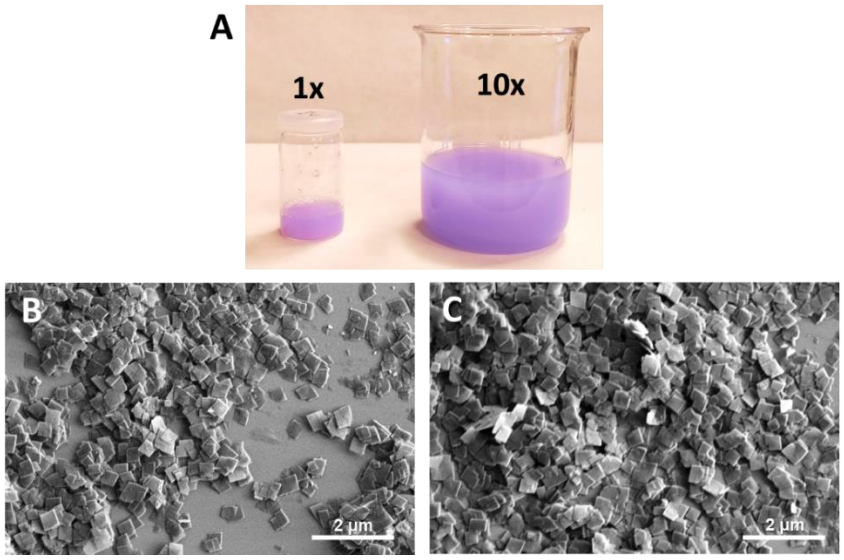

Fig. S3. Scaling-up the 2DCIFs synthesis. (A) Photographs of the 2DCIFs nanosheets prepared in small-scale (1x) that yielded 12 mg of nanosheets, and large-scale (10x) that yielded a total of 105 mg of material. (B) SEM image of nanosheets prepared in small-scale. (C) SEM image of nanosheets prepared in large-scale.

III. Structural characterization of 2DCIFs

III.1. Scanning and Transmission Electron Microscopies (SEM and TEM). The morphology (shape and size) and the homogeneity of the as-prepared 2DCIFs particles were investigated with SEM and TEM. Representative images of the 2DCIFs nanosheets prepared under optimized conditions are shown in Fig. S4, and time evolution is shown in Fig. S5. TEM-EDX (Fig. S6) and SEM-EDX mapping analysis (Fig. 1E) were used to analyse the elemental composition of the nanosheets.

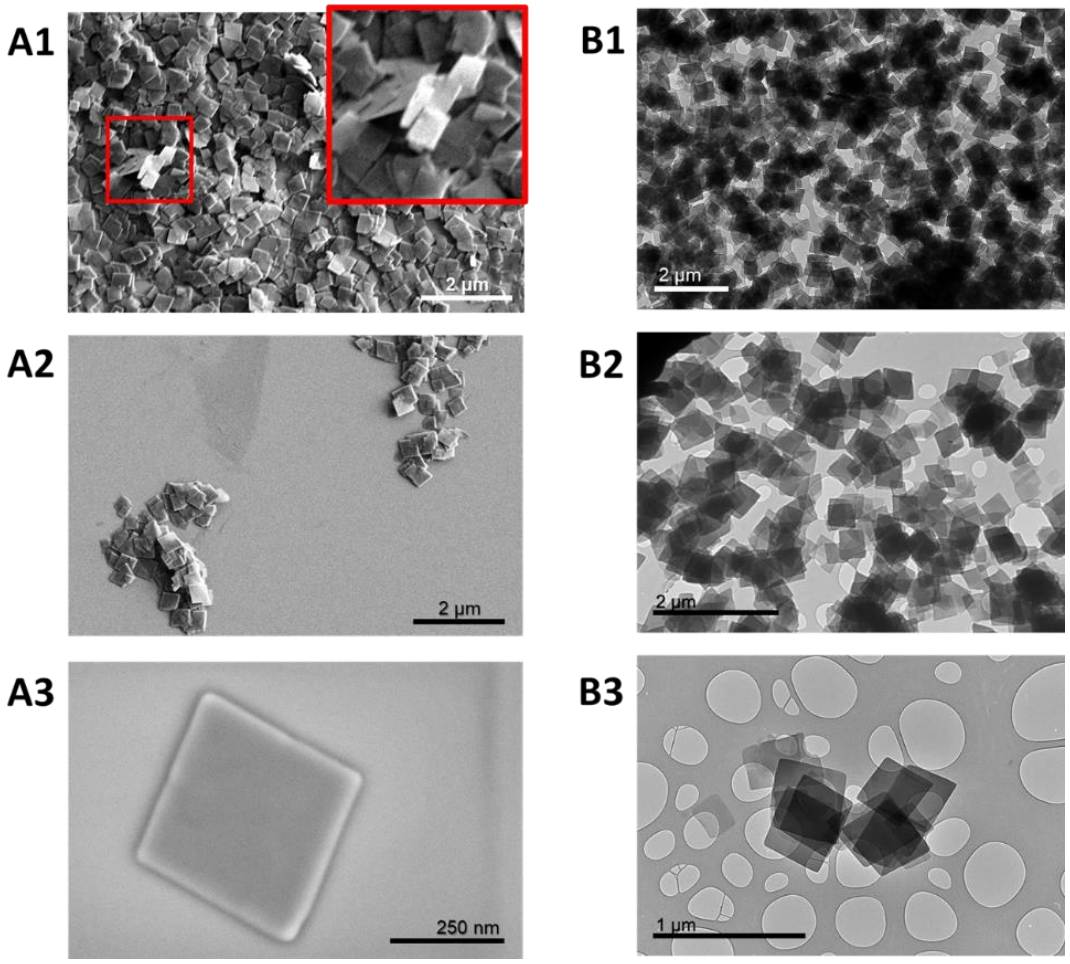

Fig. S4. (A1-A3) SEM images of the as-synthesized 2DCIFs particles; A1 shows a magnification (inset) of some nanosheets vertically-deposited (marked with a red square) to visualize the low thickness of the nanosheets. (B1-B3) TEM images of 2DCIFs; B3 shows a visible transparency across stacked sheets, which is possible due to the ultrathin nature of the nanosheets.

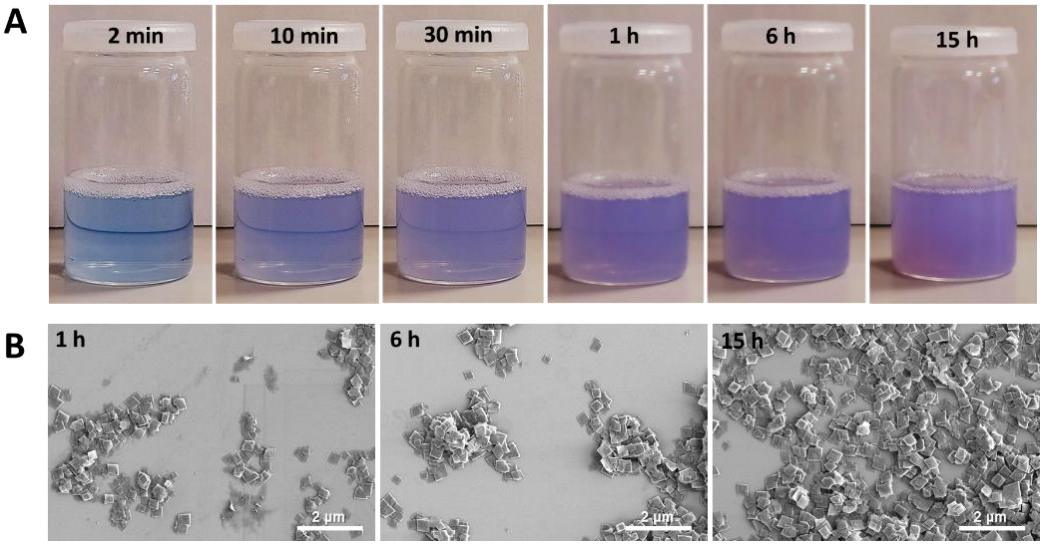

Fig. S5. (A) Photographs of the evolution over time of the reaction mixture for the synthesis of 2DCIFs. (B) SEM images of the 2DCIFs nanosheets obtained after different reaction times.

TEM coupled with energy-dispersive X-ray spectroscopy (EDX) analysis was used to qualitatively analyse the composition of the nanosheets (Fig. S6), showing the strong peak corresponding to Cu atoms.

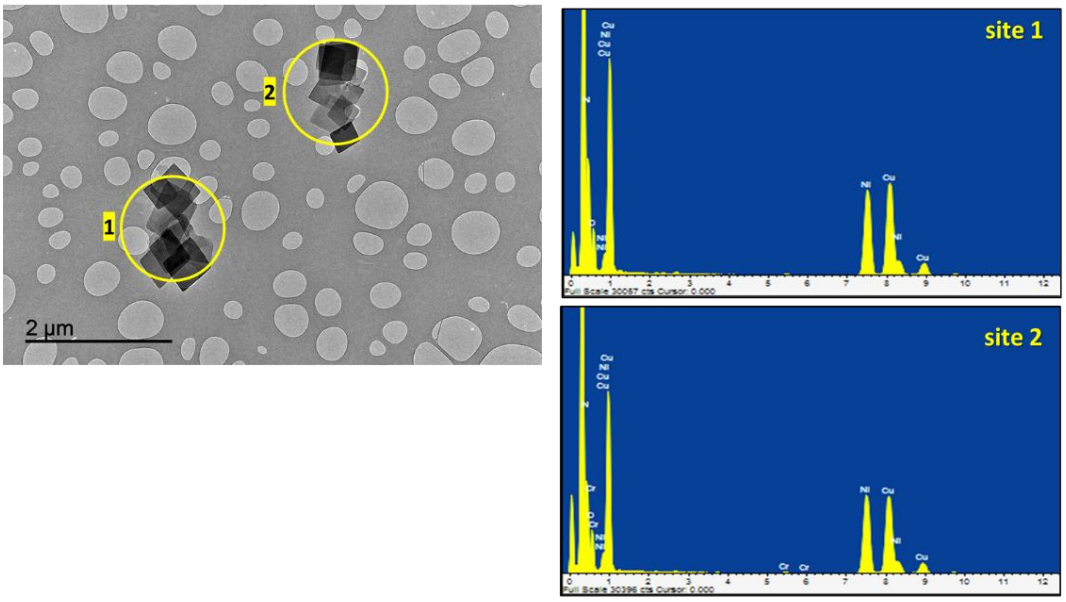

Fig. S6. EDX spectra of the corresponding measure spots in the TEM image of 2DCIFs (nickel element is due to the TEM grid).

III.2. High-Angle Annular Dark-Field Scanning Transmission Electron Microscopy (HAADF-STEM). The energy dispersive spectroscopy (EDS) in combination with HAADF-STEM technique was used to obtain element mappings and figure out the distribution of the elements in the sample. A representative EDX-STEM mapping is shown in Fig. S7, observing a homogenous distribution of all the elements in the sample. The analysis of the accumulative EDX spectrum of a single sheet gave us the chemical composition of the sample, see Table S1. Importantly, these values are consistent with those obtained by XPS.

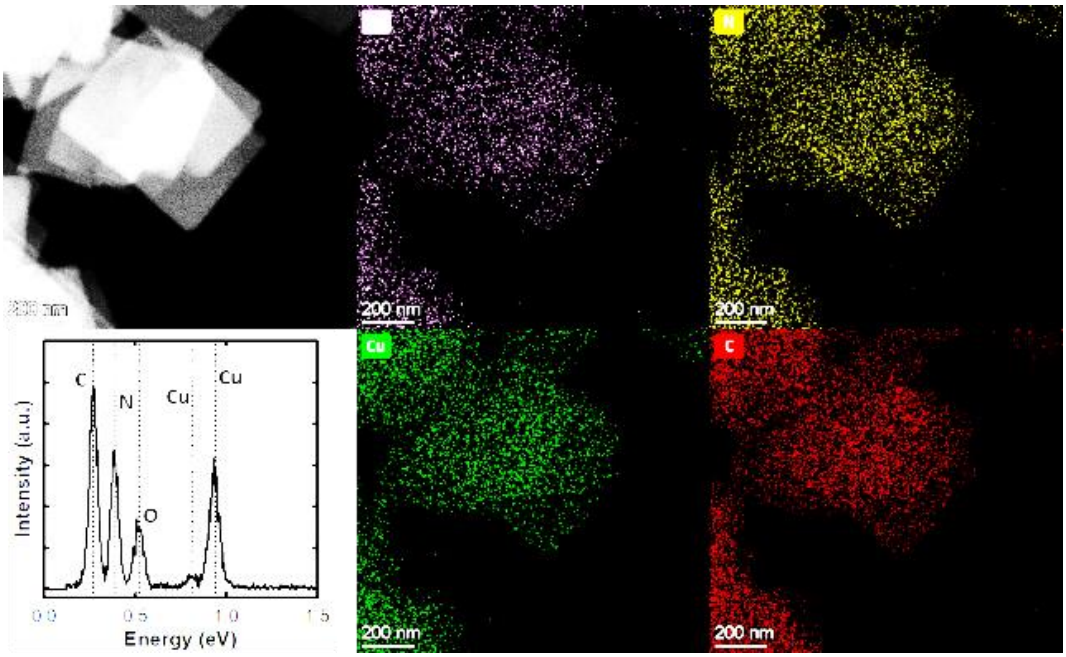

Fig. S7. HAADF-STEM image and EDX elemental mapping displaying the uniform distribution of O (purple), Cu (green), N (yellow), and C (red) in the nanosheets.

Table S1. Atomic concentration percentages from EDX-STEM analysis.

Element	Atomic %	error
Cu	6.1	1.1
O	10.7	2.4
N	25.6	5.8
C	57.6	5.9

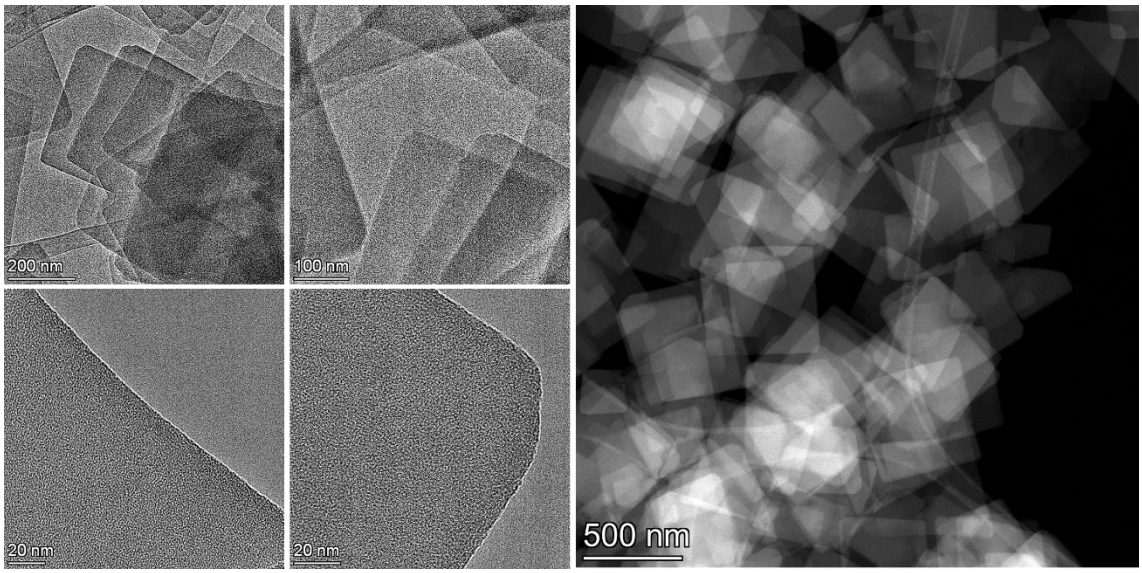

Fig. S8. Some representative HRTEM and HAADF-STEM images of the 2DCIFs.

MOFs are recognized as material highly sensitive to the electron beam and its study by TEM is really complex. In order to demonstrate the atomic dispersion of the copper atoms, high resolution HAADF-STEM images were recorded at high magnification.

Fig. S9 shows the evolution of the one area a nanosheet during the time that it was recorded. At the beginning we observed the presence of small brilliant dots that can be related with the presence of atomic Cu. However, after long irradiation time, we could observe the formation of copper particles of different sizes, as clearly observed in the image taken at 180 s. However, despite the instability of the sample under the electron beam, we can conclude that Cu was initially atomically dispersed as expected considering the determined crystal structure of 2DCIFs.

Fig. S10 shows also the effect of the electron beam irradiation on the nanosheets at low magnification.

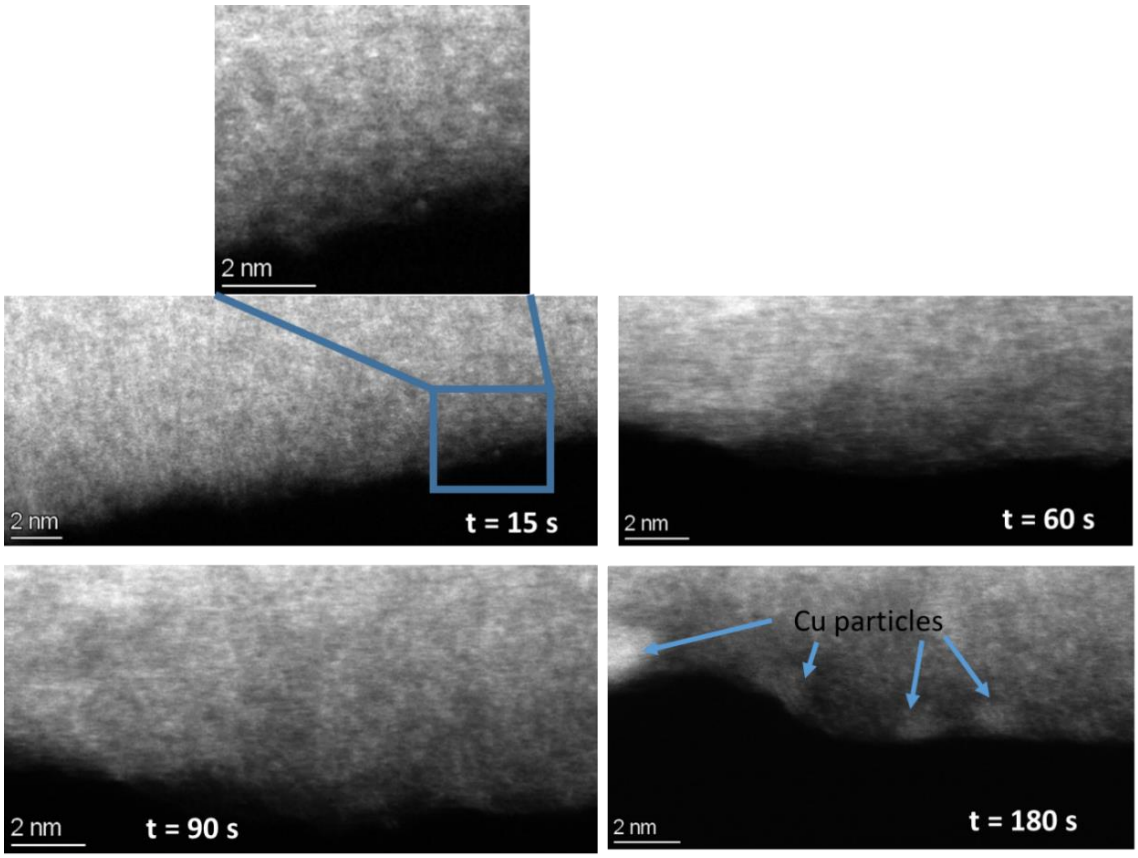

Fig. S9. HAADF-STEM images at high magnification of a small area of a nanosheet, taken over time to check the evolution during electron beam irradiation.

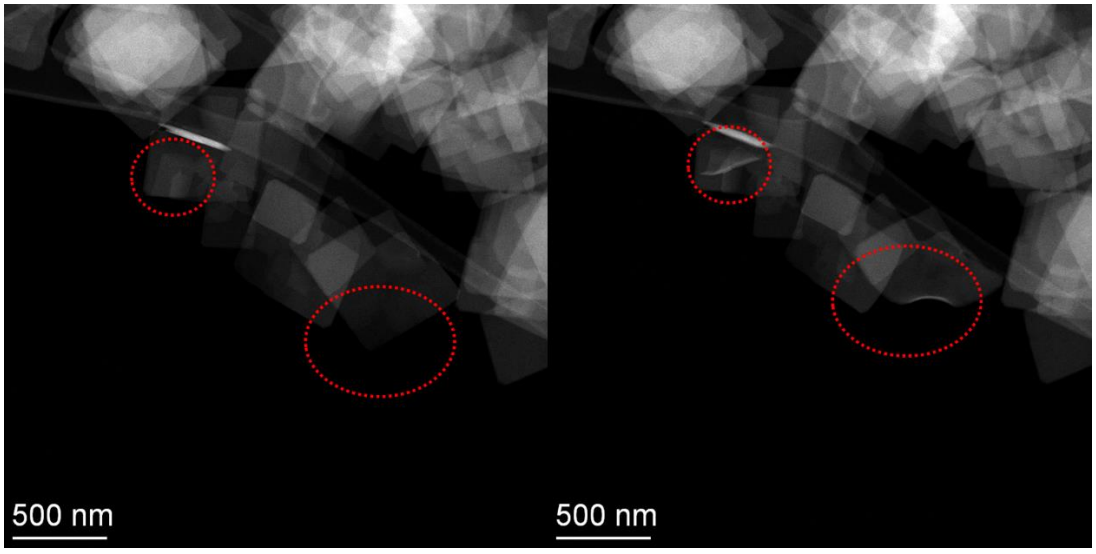

Fig. S10. HAADF-STEM images at low magnification showing the effect of the electron beam irradiation on the nanosheets; red circles indicated the changes observed between t=0 (left image) and long exposure time (right image).

.

III.3. Dynamic Light Scattering (DLS) and Zeta-Potential (ζ). DLS measurements were used to measure the hydrodynamic diameter, which corresponds to the lateral length of the nanosheets as they are 2D particles. The hydrodynamic size values obtained are in good agreement with those found by SEM and TEM. Note that the hydrodynamic length of the 2DCIFs dispersed in methanol (497 ± 9) nm is slightly greater than the average value of the dried 2DCIFs (470 ± 30) nm as determined by TEM images, which is the expected finding due to the solvation layer present when the particles are in solution. Comparison of intensity, volume and number-weighted size distributions are shown in Fig. S11 and Table S2. Moreover, the low polydispersity index of the sample clearly indicated a high particle homogeneity, which was already observed by SEM and TEM. On the other hand, LDA allowed to determine the surface charge of the nanosheets dispersed in water, obtaining a value of ζ = 7.9 ± 0.4 mV.

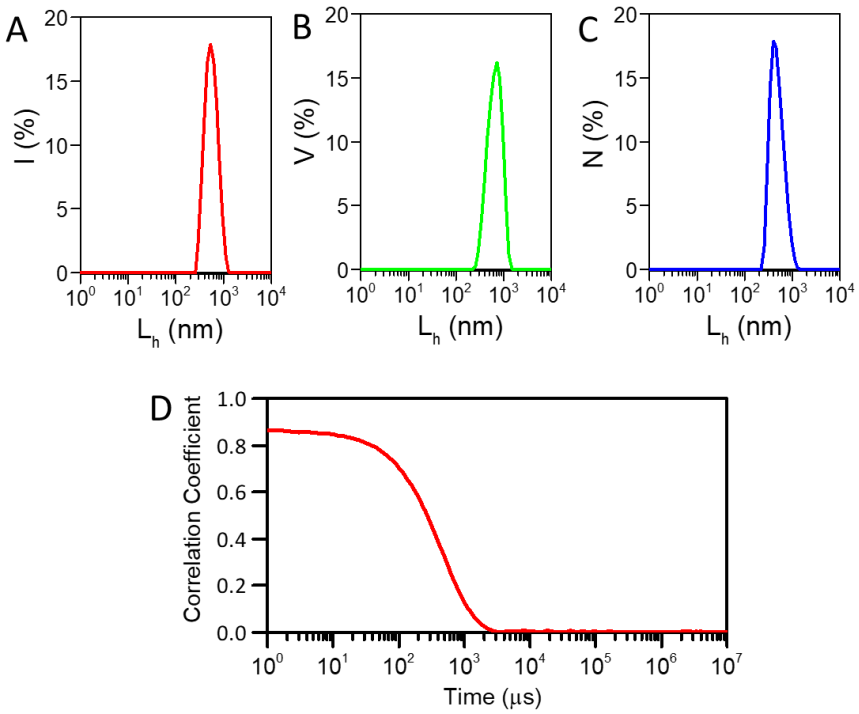

Fig. S11. DLS analysis of the 2DCIFs freshly prepared and dispersed in methanol: (A) size distribution by intensity; (B) size distribution by volume; (C) size distribution by number; and (D) autocorrelation function.

Table S2. Hydrodynamic lateral length L_h (mean value ± SD) as derived from DLS size distributions by intensity, volume and number of the 2DCIFs dispersed in methanol. SD values correspond to the standard deviation of the diameter mean value as obtained from several repetitions (n=3) of the measurement. Polydispersity index (PDI) is also given.

	L_h ± SD (nm)			
Sample	**Intensity**	**Volume**	**Number**	**PDI**
2DCIFs	572± 8	673 ± 8	497 ± 9	0.137

III.4. Powder X-Ray Diffraction (PXRD). X-ray analysis of the powder sample of 2DCIFs revealed crystalline nature of the nanosheets. The obtained diffraction pattern is shown in Fig. S12. The high crystallinity of the sample allowed us to determine the structure of the 2DCIFs nanocrystals from PXRD data, which was further confirmed by Rietveld refinement (see section IV).

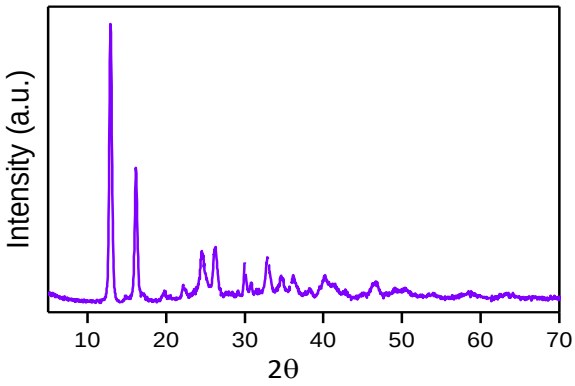

Fig. S12. Experimental PXRD spectrum from powder 2DCIFs.

III.5. Fourier-Transform Infrared Spectroscopy (FTIR). The same FTIR peaks (Fig. S13) were found for 2DCIFs samples prepared from different copper salts as well as at different reaction volume (scale), proving that all these samples have the same bond structure, consistent with the same crystallinity obtained by PXRD and the same morphology shown by SEM. On the other hand, differences between the organic liker ICA and the MOF could be clearly observed, confirming the formation of the framework. The absence of peaks related to CTAB in the FTIR spectrum of the 2DCIFs revealed the successful removal of the structuring agent (CTAB) during the purification procedure.

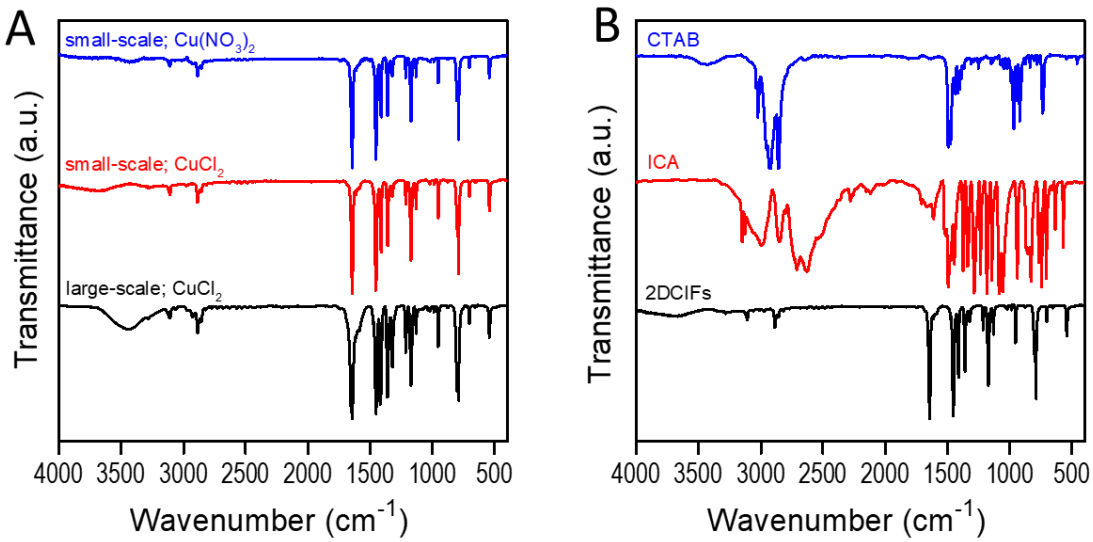

Fig. S13. (A) FTIR spectra for 2DCIFs synthesized at small-scale (1x) and large-scale (10x) using $CuCl_2$ as copper precursor. Spectrum of 2DCIFs obtained with $Cu(NO_3)_2$ as copper precursor is also shown. (B) Comparison of the FTIR spectra of the organic compounds used for the synthesis and the resulting 2DCIFs particles.

III.6. N_2 physisorption. The N_2 isotherms of the 2DCIFs nanosheets and the calculated textural properties are shown in Fig. S14 and Table S3, respectively. 2DCIFs showed mesoporous with an average pore size of 29 nm as determined from BJH pore size distributions curve.

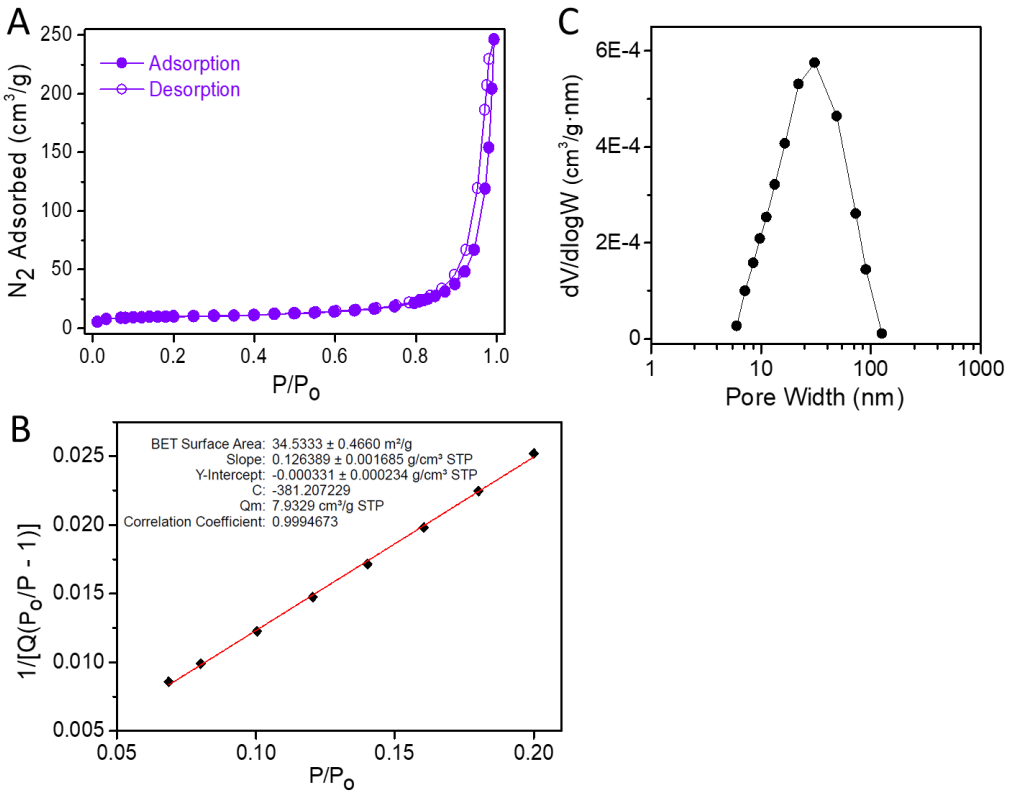

Fig. S14. (A) Experimental N_2 adsorption and desorption isotherms for 2DCIFs at 77 K. (B) Plot of the linear region for the BET equation with P/Po between 0.05 and 0.2. (C) BJH pore size distributions curve of 2DCIFs.

Table S3. Textural properties of 2DCIFs nanosheets.

Sample	S_{BET} ($m^2 \cdot g^{-1}$)	V_{micro} ($cm^3 \cdot g^{-1}$)	V_{meso} ($cm^3 \cdot g^{-1}$)
2DCIF nanosheets	34.5 ± 0.5	0.007	0.177

S_{BET}: Surface area calculated by BET equation; Vmicro and Vmeso: micropore and mesopore volume (P/P_0 =0.9) calculated by V-t method.

III.7. Thermogravimetric analysis (TGA) The thermal stability of the 2DCIFs nanosheets was tested by thermogravimetric analysis. In the Fig. S15 it could be seen two main mass loss steps. The lower temperature peak at 280 °C, which corresponds to a mass change of about 28 %, may be due to conversion of carbonyl groups (C=O) to either CO or CO_2. The second mass loss (with a mass change of about 41 %) appearing in the range of 320 to 400 °C is related to the disintegration of the MOF structure. The residue mass remaining at the end of the analysis (31.3 wt%) is due to the oxidation of Cu metal to CuO, which corresponds quite well with the theoretical calculations by assuming an empirical formula of $Cu(ICA)_2$. It must be noted that TGA plot revealed the absence of occluded and/or adsorbed solvent molecules used during synthesis

and/or purification, which is a common issue in most of the MOFs that makes necessary a further thermal step to activate the MOFs by removing such molecules. This finding indicates that a thermal activation step is not required for these 2D MOFs. The ultrathin 2D structure is likely responsible of the easy and complete removal of solvent molecules by the optimized method, which involves a solvent-exchange procedure with methanol during purification, and the further evaporation of methanol under mild condition (vacuum-drying at 60 °C for 18 h).

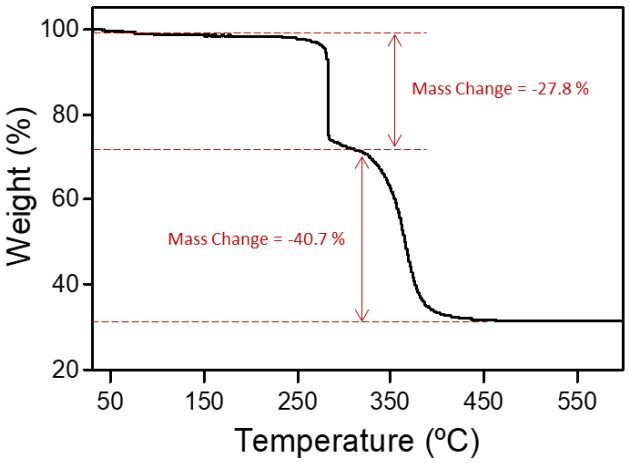

Fig. S15. Thermogravimetric analysis of 2DCIFs nanosheets recorded in a dynamic air atmosphere.

III.8. X-ray Photoelectron Spectroscopy (XPS). XPS analyses were performed not only to confirm the stoichiometry of the $Cu(ICA)_2$ structure, but also to demonstrate the absence of chloride anions in the network through inferring the chemical composition and states of the 2DCIFs. For this, different syntheses of the nanosheets were carried out by varying the molar ratio of its constituent components (1:1 and 1:2 of $CuCl_2$/ICA), and other synthesis was performed by using a different copper salt as precursor, *i.e.* $Cu(NO_3)_2$ instead of $CuCl_2$ (Fig. S16A), while maintaining the optimized synthetic conditions described above (see section II.1). Fig. S16B shows the resulting survey spectrum obtained for the different as-prepared samples, demonstrating clearly that the chemical composition was practically identical despite of varying the molar ratio between the metallic precursor and the organic ligand from 1:1 to 1:2, as well as using a different salt of the same metallic precursor. The main peaks located at binding energies (BEs) of approximately 934.3, 530.9, 398.5, and 286.2 eV in the survey scans are attributed to Cu 2p, O 1s, N 1s, and C 1s, respectively.[3] The obtained high-resolution XPS spectra of Cu 2p, N 1s and C 1s for the resulting 2DCIFs synthesized using different ratio of its constituent components and varying the copper salt are given in Fig. S17 and S18.

Finally, in order to quantify the stoichiometry of the 2DCIFs, the atomic concentration percentages of the different chemical elements were obtained from these XPS data (Table S4). It should be noted that the theoretical O/Cu and N/Cu ratios for a $Cu(ICA)_2$ structure were 2 and 4, respectively. In summary, all these observations are in good agreement with the proposed $Cu(ICA)_2$ structure for the 2DCIFs.

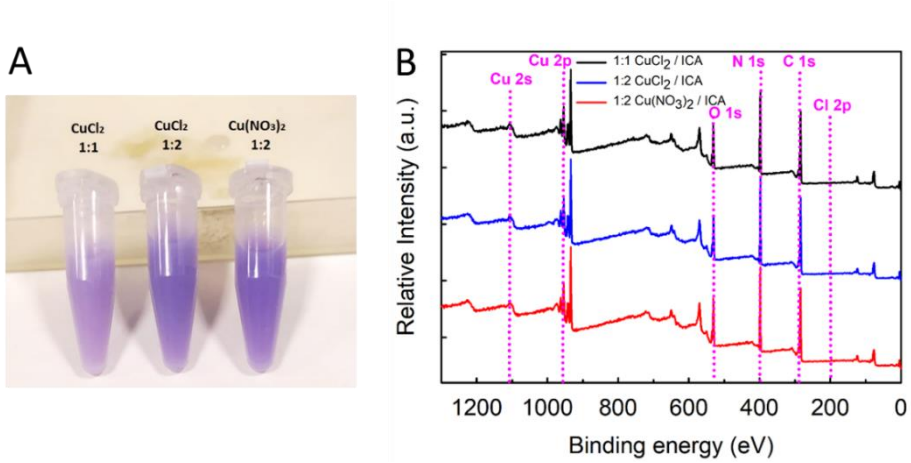

Fig. S16. (A) Photographs of the different 2DCIFs samples used for the XPS analysis. which were obtained employing the optimized synthesis conditions. (B) Comparative XPS survey spectra from 2DCIFs obtained using two different molar ratios of its constituent components, $CuCl_2$ and ICA (1:1 and 1:2), and another one using $Cu(NO_3)_2$ as salt precursor in a molar ratio of $Cu(NO_3)_2$:ICA.

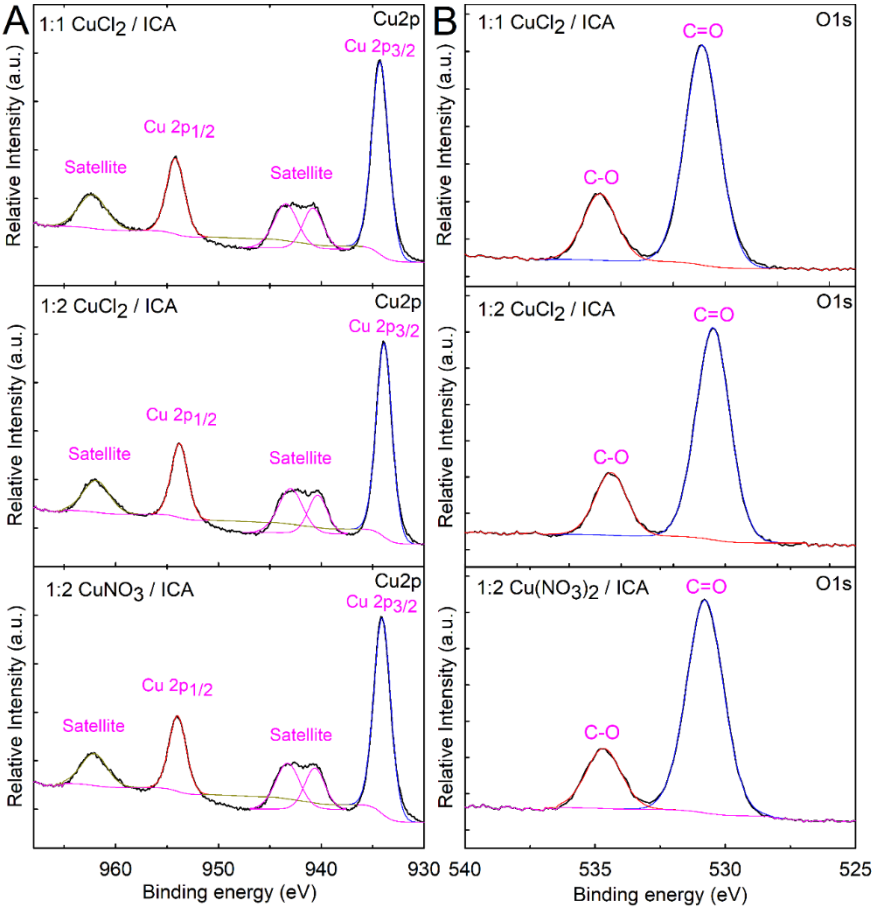

Fig. S17. (A) High-Resolution (HR) XPS spectra of Cu 2p for the resulting 2DCIFs synthesized using different ratio of its constituent components (1:1 and 1:2 of $CuCl_2$/ICA) and varying the salt of the same metallic precursor ($CuCl_2$ versus $Cu(NO_3)_2$). (B) HR XPS spectra of O 1s for the same samples.

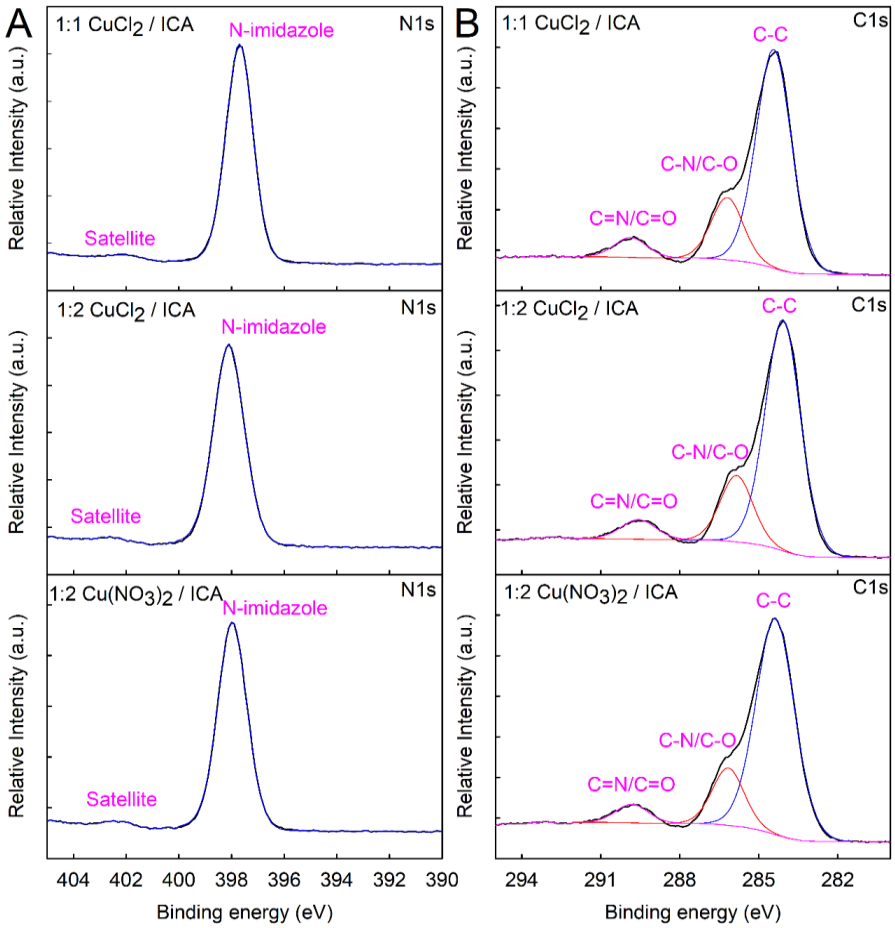

Fig. S18. (A) HR XPS spectra of N 1s for the resulting 2DCIFs for the resulting 2DCIFs synthesized using different ratio of its constituent components (1:1 and 1:2 of $CuCl_2$/ICA) and varying the salt of the same metallic precursor ($CuCl_2$ versus $Cu(NO_3)_2$). (B) HR XPS spectra of C 1s for the same samples.

Table S4. Atomic concentration percentages from XPS analysis.

Sample	Cu	O	N	C	O/Cu	N/Cu
1:1 $CuCl_2$ / ICA	5.4	12.9	26.4	55.4	2.3	4.8
1:2 $CuCl_2$ / ICA	5.1	13.1	26.7	55.1	2.5	5.2
1:2 $Cu(NO_3)_2$ / ICA	5.0	13.2	26.7	55.1	2.6	5.3

III.9. Chemical stability. DLS measurements over time were carried out to investigate the colloidal stability of the in different media, *i.e.,* methanol, water, and KOH 0.1 M. Unfortunately, 2DCIFs were not stable in acidic media (H_2SO_4) as expected due to pKa value of ICA ligand. Data plotted in Fig. 1C are summarized in Table S5. Fig. S19 shows SEM images after one month of the 2DCIFs nanosheets dispersed in the different studied media.

Table S5. Hydrodynamic lateral length L_h (mean value ± SD) as derived from DLS measurements (size distribution by number) of the 2DCIFs over time (up to 1 month) dispersed in different media (MeOH, H_2O, and KOH 0.1M). SD values correspond to the standard deviation of the diameter mean value as obtained from several repetitions (n=3) of the measurement.

	L_h ± SD (nm)		
Time (days)	**MeOH**	**H_2O**	**KOH**
0	497 ± 9	499 ± 10	494 ± 9
1	501 ± 10	487 ± 14	533 ± 8
7	499 ± 9	466 ± 15	539 ± 7
14	504 ± 10	468 ± 14	514 ± 8
30	505 ± 14	467 ± 16	519 ± 9

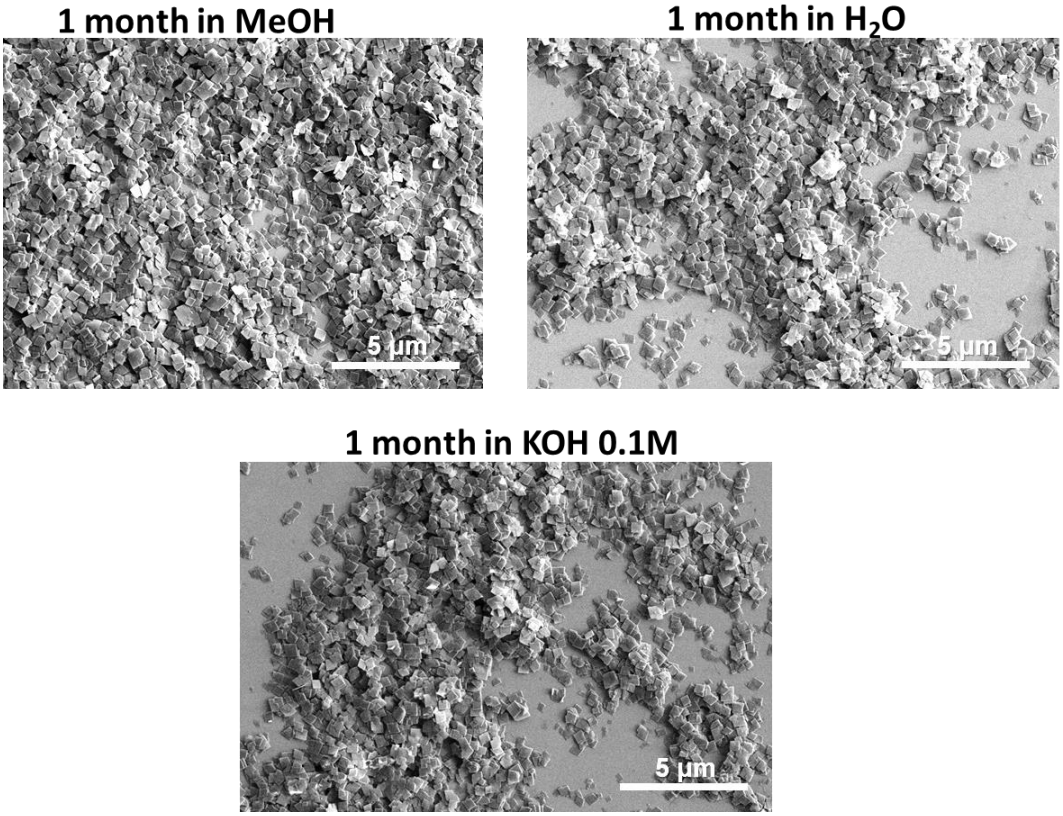

Fig. S19. SEM images of the 2DCIFs dispersed in different media (MeOH, H_2O, and KOH 0.1M) after 1 month stored at RT.

IV. Crystal structure determination by Rietveld refinement of diffraction data

The structure of the as-synthetized 2DCIFs was deduced from powder X-ray diffraction data and was confirmed by Rietveld refinement. The Rietveld refinement with energy (50%)[4] of the diffraction pattern was carried out using the Biovia/Materials Studio 2020 software (Accelrys Software Inc.: San Diego, CA 92121, USA). The Powder Refinement module of Materials Studio allows to optimize powder diffraction simulation parameters and crystal structures to obtain the best possible agreement between simulated and experimental powder patterns. Previously, the baseline was subtracted using the algorithm developed by Bruckner.[5] Universal Force Field (UFF)[6] as implemented in Forcite module of Materials Studio was used to optimize the energy (50% of weight in fit). Fig. S20 shows the experimental diffraction pattern for 2DCIFs nanosheets, calculated and difference pattern. The final figures of merit were: R_{wp} = 5.33 %, R_p = 10.17 %, CMACS = 0.40 % (2θ range 10°-45°). Lattice parameters, fractional coordinates, assignment of diffraction peaks, anisotropic temperature factors and pattern parameters are given in Tables S6-S10.

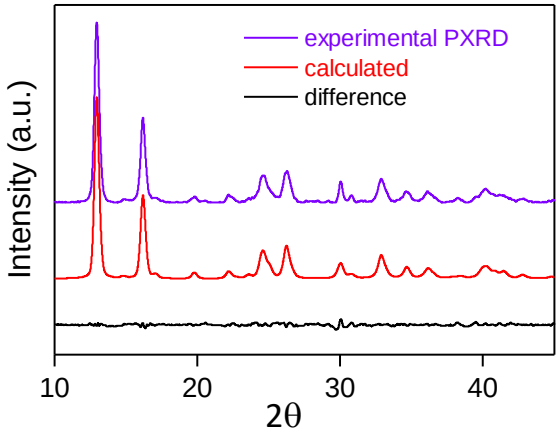

Figure S20. Experimental PXRD spectrum (violet) from powder 2DCIFs is compared is compared against the calculated pattern (red) from the structural model and their difference (black). *R* factors in the Rietveld refinement: R_{wp} = 5.33 %, R_p = 10.17 %.

Table S6. Crystal Data details for 2DCIFs. More parameters are given in annex 1.

Empirical Formula	$CuC_8H_6N_4O_2$
Crystal system	monoclinic
Space group	*P*1*c*1
Unit Cell Dimensions	
a (Å)	5.434(8)
b (Å)	5.969(9)
c (Å)	14.25(2)
α (°)	90
β (°)	107.156(9)
γ (°)	90

Table S7. Fractional Coordinates.

No.	Name	u	v	w	Refined?
1	Cu	-0.13263	0.46554	0.57765	Yes
2	C	0.37736	0.43409	0.54750	Yes
3	N	0.13123	0.34738	0.50991	Yes
4	N	0.48199	0.52233	0.47848	Yes
5	C	0.49910	0.42725	0.65198	Yes
6	C	0.07960	0.38307	0.41231	Yes
7	C	0.29297	0.48938	0.39338	Yes
8	O	0.71355	0.50073	0.70047	Yes
9	H	0.37155	0.34227	0.69074	Yes
10	H	-0.10381	0.33315	0.36027	Yes
11	H	0.31473	0.54308	0.32287	Yes
12	C	0.85406	0.94718	0.53400	Yes
13	N	0.81787	1.11574	0.59549	Yes
14	N	1.03180	0.78655	0.57905	Yes
15	C	0.70686	0.95183	0.43178	Yes
16	C	0.98181	1.05750	0.68351	Yes
17	C	1.11158	0.85745	0.67335	Yes
18	O	0.71870	0.82453	0.36396	Yes
19	H	0.56400	1.09386	0.41622	Yes
20	H	1.00067	1.15781	0.74948	Yes
21	H	1.25512	0.76406	0.72985	Yes

Table S8. Assignment of the resulting diffraction peaks.

2-θ exper.	(h, k, l) assignment			2-θ theor.	I / I_{max}	Mult.	2-θ exper.	(h, k, l) assignment			2-θ theor.	I / I_{max}	Mult.
12.950	0	0	2	12.978	100	2		1	2	0	34.741	3.61	4
14.886	0	1	0	14.830	1.06	2		1	2	-2	35.306	0	4
16.185	0	1	1	16.207	49.41	4		1	0	4	35.648	0.02	2
17.127	1	0	0	17.045	2.3	2		1	1	-5	35.745	0.5	4
	1	0	-2	18.115	0.02	2	36.115	0	2	3	36.107	7.35	4
19.811	0	1	2	19.788	3.75	4		0	1	5	36.342	1.15	4
22.184	1	1	-1	22.157	4.53	4		1	2	1	36.371	0.04	4
	1	1	0	22.701	1.07	4		2	1	-2	36.459	1.51	4
	1	1	-2	23.525	1.97	4		2	1	-1	36.536	0.52	4
24.562	1	0	2	24.468	11.01	2		2	0	-4	36.797	0.04	2
24.645	0	1	3	24.669	10.47	4		1	2	-3	37.451	0.03	4
	1	1	1	25.038	6.93	4		2	1	-3	37.612	0.05	4
26.288	0	0	4	26.210	21.19	2		2	1	0	37.836	0.54	4
	1	1	-3	26.527	5.59	4	38.224	1	0	-6	38.343	2.39	2
	1	0	-4	26.717	0	2		1	1	4	38.833	0	4
	1	1	2	28.764	0	4		1	2	2	39.128	0.03	4
30.038	0	2	0	30.002	11.8	2		0	0	6	39.818	1.31	2
	0	1	4	30.278	0.01	4	39.577	2	1	-4	39.904	5.71	4
	1	1	-4	30.724	0.12	4	40.188	2	1	1	40.259	7.45	4
30.770	0	2	1	30.734	2.96	4		0	2	4	40.297	0.83	4
32.877	0	2	2	32.840	16.59	4		1	2	-4	40.646	0.15	4
	2	0	-2	33.080	4.48	2		2	0	2	40.780	4.25	2
	1	1	3	33.461	0	4	41.157	1	1	-6	41.352	6.3	4
	1	2	-1	34.374	0.17	4		0	1	6	42.740	3.42	4
34.605	2	0	0	34.573	6.05	2		1	2	3	42.833	0	4

Table S9. Anisotropic temperature factors.

No.	Name	U_{eq}	U_{11}	U_{22}	U_{33}	U_{12}	U_{23}	U_{13}	Refined?
1	Cu	19.2896	22.8306	20.7006	21.9160	-19.6956	-18.5304	18.3274	Yes
2	C	4.7642	3.1229	10.3996	0.7948	0.7726	1.5747	0.6161	Yes
3	N	9.2691	21.7081	2.6736	8.1196	0.2361	-1.0302	11.6634	Yes
4	N	7.8303	7.7961	3.2665	10.2104	1.6546	1.48789	-0.7764	Yes
5	C	17.0777	3.7143	1.6212	44.4685	1.1078	-0.4586	4.8953	Yes
6	C	12.3864	3.8821	8.2812	27.0760	4.5285	12.3584	7.7852	Yes
7	C	8.0847	4.2993	18.5394	0.9032	7.1953	-1.9585	-0.02509	Yes
8	O	7.1471	5.9219	14.5007	1.0623	0.7473	3.3443	1.0973	Yes
9	H	3.0683	2.2858	6.1816	1.5084	-1.9624	-1.6415	1.7523	Yes
10	H	2.4389	5.3965	0.1981	1.1189	-0.0205	-0.4372	0.0276	Yes
11	H	4.80340	7.03161	4.69602	3.47499	-2.2705	1.5291	2.7759	Yes
12	C	11.7386	15.4489	10.5539	12.5381	-9.48184	-6.94464	9.27381	Yes
13	N	9.6182	24.50991	1.95561	7.15741	4.15143	3.09450	12.04973	Yes
14	N	10.08938	5.4580	10.2235	15.2161	4.0549	10.0461	4.0235	Yes
15	C	10.2292	13.1692	8.6453	4.5884	-2.7003	1.2301	-4.0116	Yes
16	C	10.5325	3.2042	16.6709	10.2835	-0.4434	8.9817	-0.2371	Yes
17	C	12.5914	22.0401	0.4801	10.7451	-0.4254	0.78451	-2.1416	Yes
18	O	17.3920	3.2269	6.9346	32.5817	2.7572	-5.4769	-9.3154	Yes
19	H	2.2475	0.6793	5.1042	1.1547	-0.6303	1.0242	0.5734	Yes
20	H	2.5966	0.1336	3.6399	3.74365	-0.5994	-0.4218	0.1500	Yes
21	H	3.5093	2.4094	3.7805	4.9170	1.2890	3.8755	1.9768	Yes

Table S10. Pattern Parameters.

FWHM Profile Function: Pseudo-Voigt	**Parameter**	**Value**	**Refined?**
	U	0.75517	Yes
	V	0.22369	Yes
	W	0.12482	Yes
Profile	**Parameter**	**Value**	**Refined?**
	NA	0.09908	Yes
	NB	0.01860	Yes
Line Shift Instrument Geometry: Bragg-Brentano	**Parameter**	**Value**	**Refined?**
	Zero Point	-0.00243	Yes
	Shift #1	-0.08879	Yes
	Shift #2	0.36167	Yes
Asymmetry Correction: Berar-Baldinozzi	**Parameter**	**Value**	**Refined?**
	P1	-0.00654	Yes
	P2	-0.16369	Yes
	P3	0.02365	Yes
	P4	0.34295	Yes

Crystal structure investigations have revealed that the coordination number of Cu atoms is five with square pyramidal geometry. Each Cu center of the SBU unit is coordinated with four ICA ligands; specifically, three ICA ligand are only interacting with metal ion through a N atom while the fourth ICA is interacting with Cu through one N atom (from the imidazole ring) and the O atom (from its aldehyde group), *cf.* Fig. S21. Cu−N and Cu−O distances are in the range of other reported copper MOFs.[7,8] Perspectives along each axis of the structure (Fig. S22) revealed the existence of sheets, confirming the 2D layer structure of the 2DCIFs. As can be seen in Fig. S23, Cu atoms remain relatively exposed on one side of the layer where all the O atoms are coordinated. However, on the opposite side of the layer, the O atoms do not participate in the coordination. Solvent excluded surface (Fig. S24A) and porosity maps (Fig. S24B-D) have been obtained using CrystalMaker software. The yellow translucent sphere showing the maximum volume available within the framework, while the solvent excluded surface emphasizes the envelope around the framework.

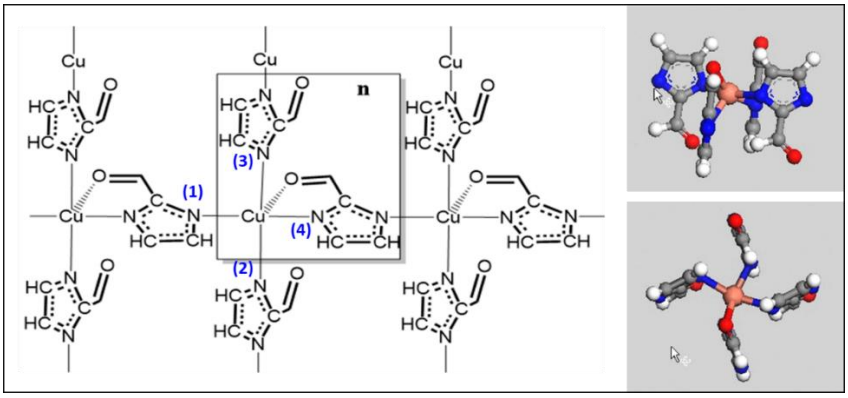

Fig. S21. Coordination mode of the Cu ion in the structure. Different perspective views are shown (color code: pink Cu, gray C, blue N, red O, white H). Most important distances are: Cu-N(1) = 2.074Å, Cu-N(2) = 2.112Å, Cu-N(3) = 2.130Å, Cu-N(4) = 2.180Å, Cu-O = 2.161Å.

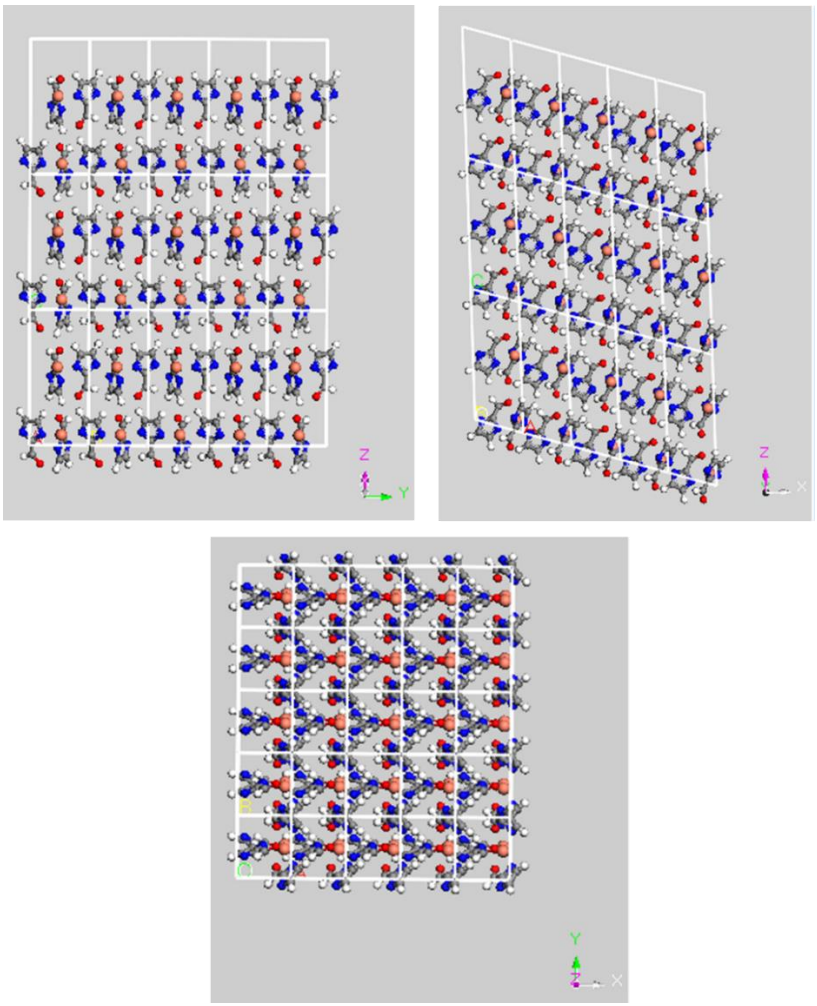

Fig. S22. Representation of the 2DCIFs along each axis (x, y and z), which confirm the 2D layer structure of the nanocrystals. Color code: pink Cu, gray C, blue N, red O, white H.

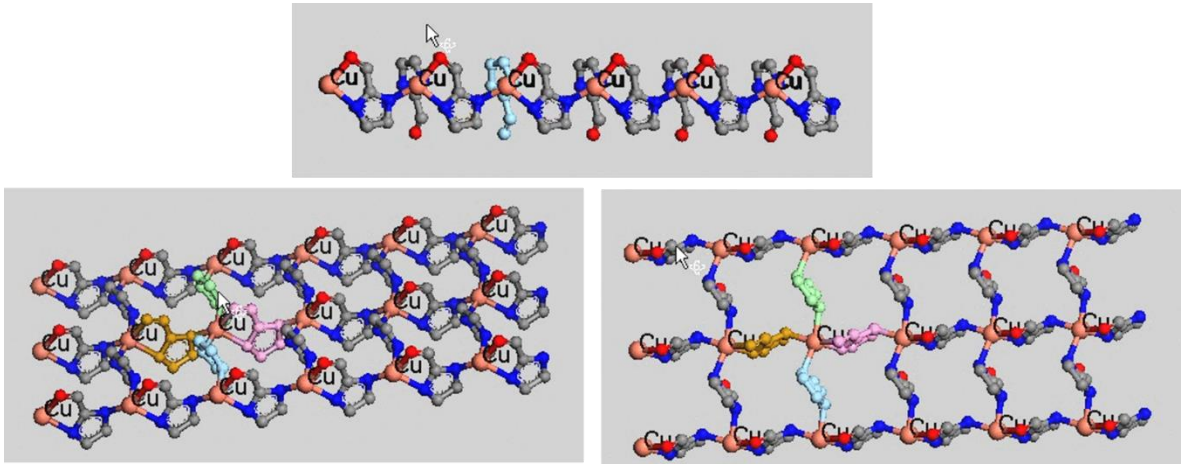

Fig. S23. Representation of the 2D layer from different perspectives, showing that O atoms are coordinated to Cu atoms on one side of the layer, leaving thus the Cu atoms relatively exposed; however, O atoms are not coordinated on the opposite side of the layer. Color code: pink Cu, gray C, blue N, red O, white H.

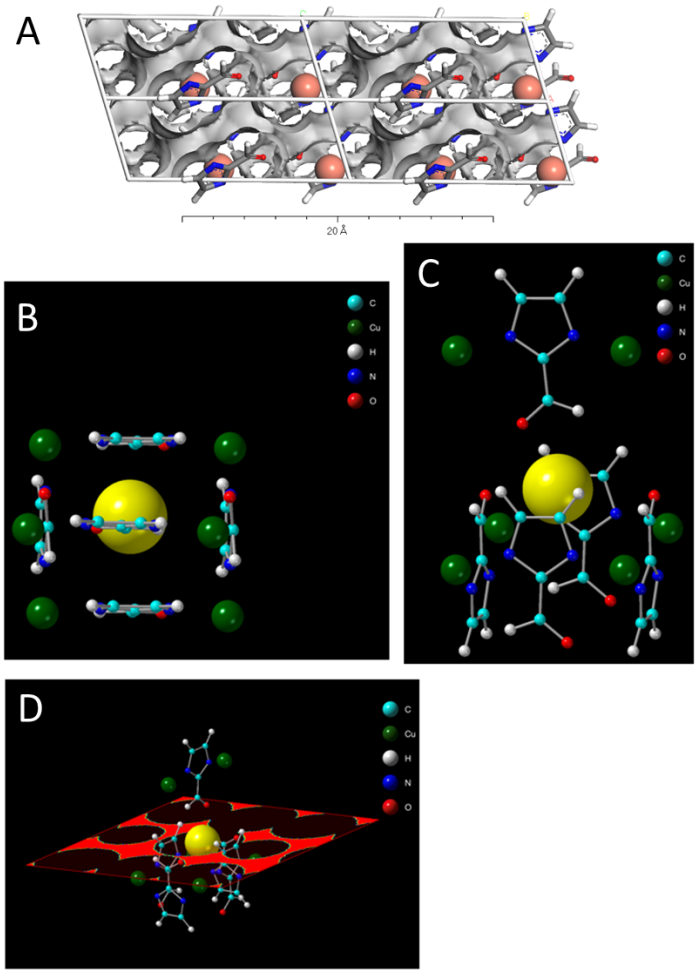

Fig. S24. (A) Three-dimensional (3D) structure of 2DCIFs showing the region accessible to water (solvent excluded surface), which allows visualizing the existence of pores within the structure. (B-C) Porosity maps showing the pore space (yellow sphere) within the crystal structure, which has a diameter of 4.6 Å.

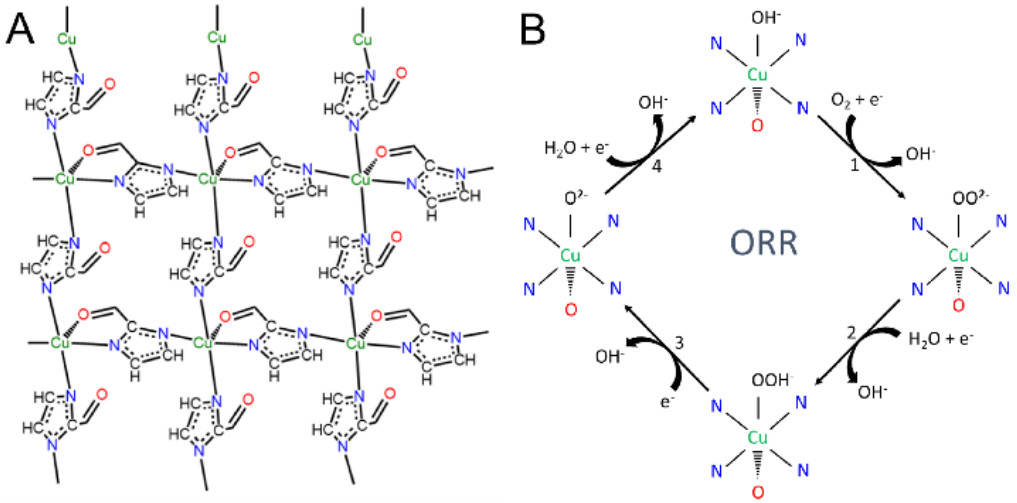

Fig. S25. (A) Schematic structure of 2DCIFs with Cu-N4O active sites, and (B) the proposed ORR mechanism.

V. Electrocatalytic performance of 2DCIFs towards ORR

V.1. Electrochemical durability tests

The durability of electrocatalysts appears one of the most important issues that has to be addressed before the commercialization of electrochemical devices for energy. The stability of 2DCIFs catalysts was evaluated using an accelerated aging test (AAT), which uses 1000 continuous potential cycles performed by CV measurements in O_2-saturated 0.1 M KOH solution.[9] Fig. S26 shows the excellent stability of this electrocatalyst material, where the slight decrease in current density would be associated with the loss of material deposited on the GCE surface after the AAT.

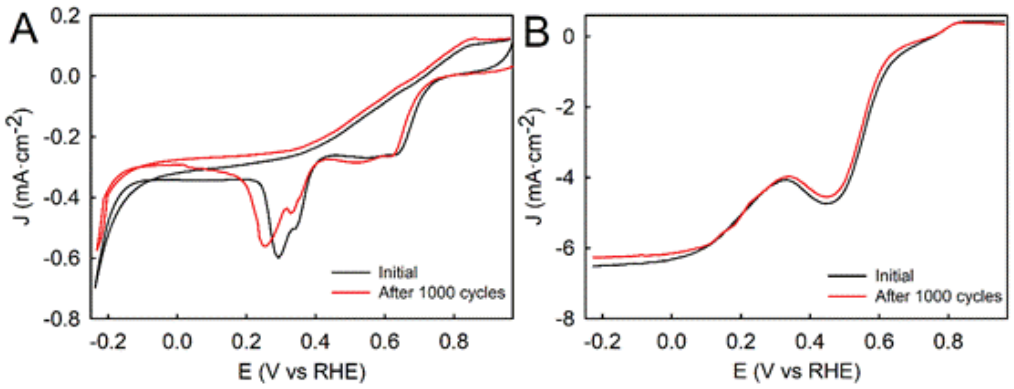

Fig. S26. Cyclic voltammograms (CVs) of GCE modified with 2DCIFs before and after 1000 cycles of the AAT, in O2-saturated 0.1 M KOH at scan rate of 10 $mV \cdot s^{-1}$: (A) Under static conditions and (B) using a rotating rate of 2500 rpm.

V.2. Characterization of 2DCIFs after the electrocatalytic process

Post-ORR characterization on the 2DCIFs was performed using SEM, XRD, and XPS analysis to check whether the morphology, the crystal structure and the chemical composition and its states were affected during the electrochemical measurements. Fig. S27 shows representative SEM images of the 2DCIFs supported onto ITO electrode before and after the ORR measurements, indicating that neither the size nor the shape of the 2DCIFs were significatively affected. The formation of 2DCIFs layer onto ITO electrode by drop-casting gave rise to the growth of the crystalline structure affected by a preferred orientation perpendicular to the ITO surface, observing the peaks corresponding to the 00k planes, preferentially. Of these, the peak assigned to plane 002 was the most intense. Fig. S28 shows this peak for the freshly prepared sample, as well as for the sample after 1 and 5 ORR cycles. As can be seen, both the position (~ 13°) and the FWHM of the peak remain constant, indicating that the crystal structure (actually the inter plane spacing c = 1.425 nm) is preserved after the ORR cycles performed. Fig. S29 compares the survey XPS spectra of the 2DCIFs before and after the ORR analysis, highlighting the presence of potassium (K 3s peak) from the electrolyte solution in the latter case, and some new peaks from the ITO electrode due to the material loss during ORR measurements. The

obtained high-resolution XPS spectra of Cu 2p, N 1s and C 1s for the 2DCIFs before and after the ORR process are given in Fig. S30 and S31.

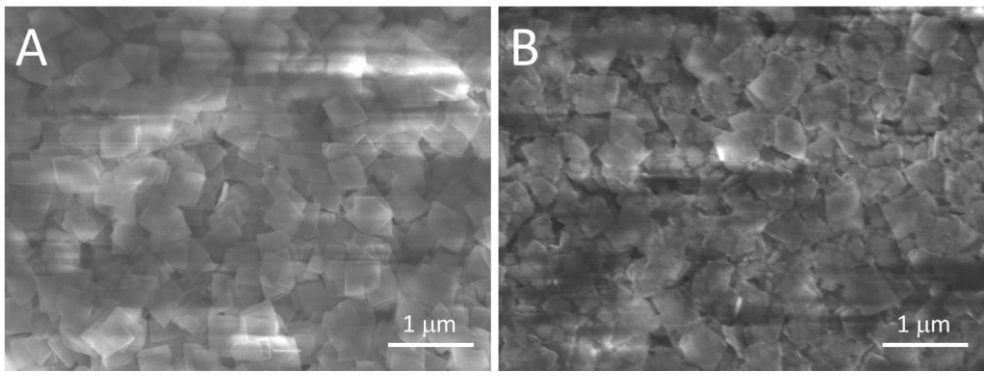

Fig. S27. Representative SEM images of the 2DCIFs drop-casted onto ITO electrode. (A) Before and (B) after ORR electrochemical analysis.

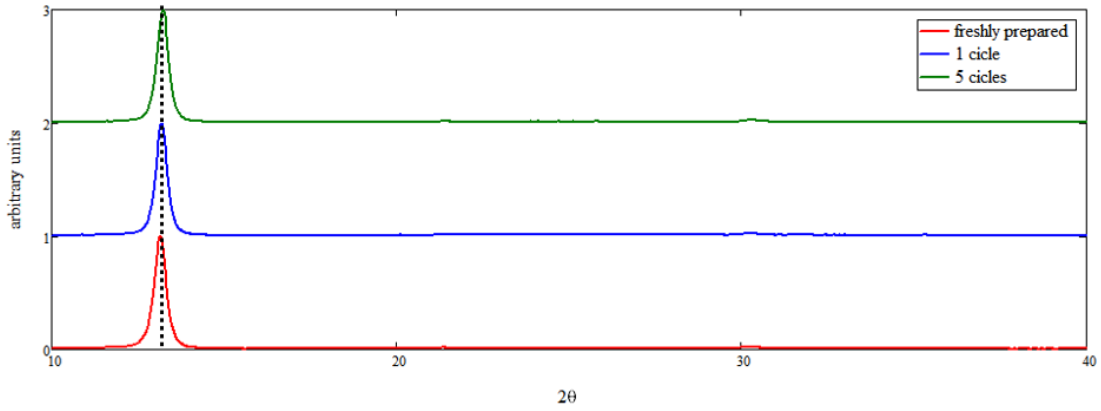

Fig. S28. XRD diffractograms of 2DCIFs-modified ITO, before (red line) and after one (blue line) and five (green line) CV scans.

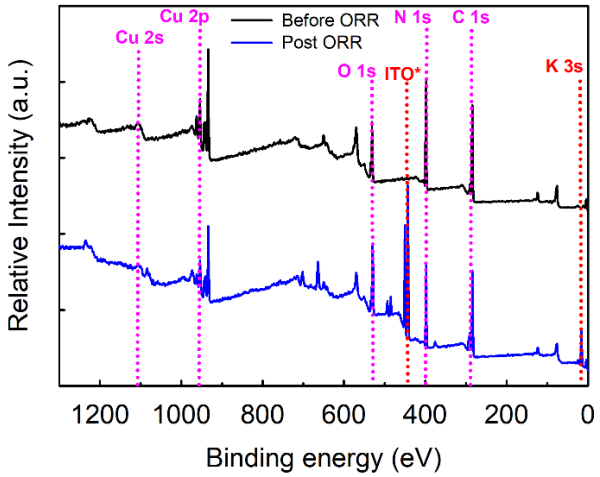

Fig. S29. Survey XPS spectra of the 2DCIFs drop-casted onto an ITO electrode, before (black line) and after (blue line) ORR electrochemical analysis.

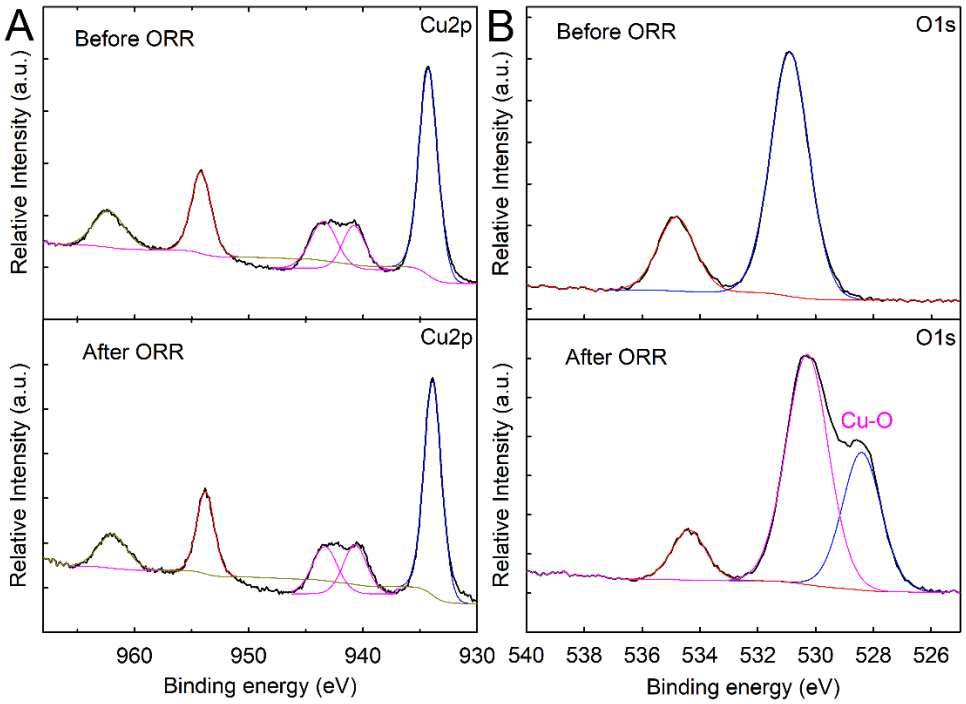

Fig. S30. High-Resolution XPS spectra of Cu 2p (A) and O 1s (B) for the 2DCIFs before and after the ORR electrochemical analysis.

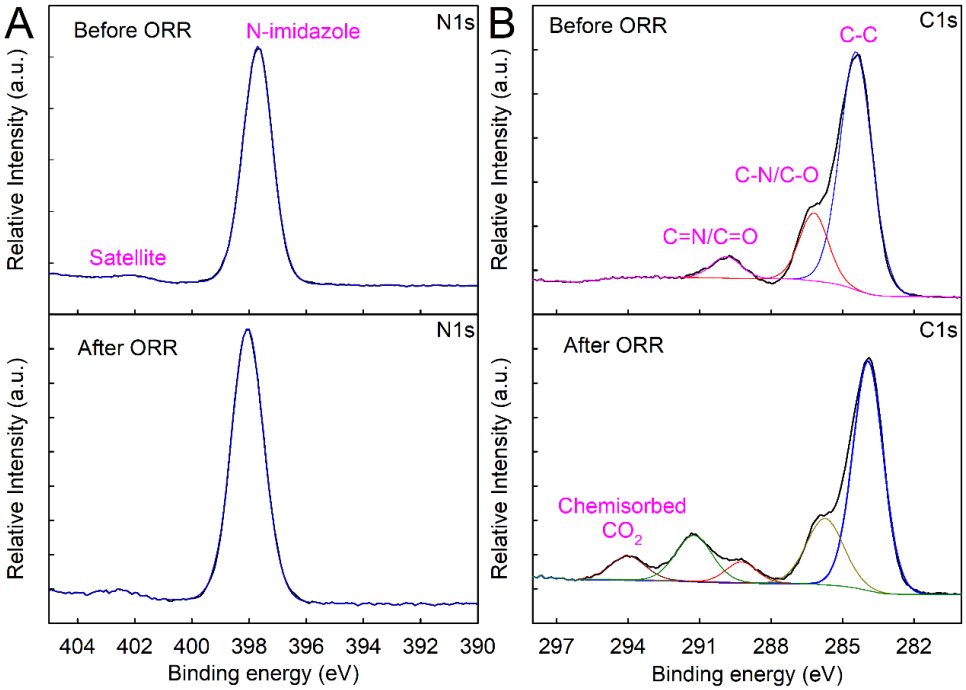

Fig. S31. High-Resolution XPS spectra of N 1s (A) and C 1s (B) for the 2DCIFs before and after the ORR electrochemical analysis.

V.3. Comparison of different Cu-based MOFs or MOF-derived Cu/C materials for ORR

Table S11. Comparison of ORR performance of Cu-based MOFs or MOF-derived Cu/C materials

Catalyst name	MOF structure	Metal composition	E_{onset} (mV)	$E_{1/2}$ (mV)	J_{max} ($mA \cdot cm^{-2}$)	Electron transfer number	Electrolyte	Working Electrode	Ref.
2DCIF	Yes; pristine	Cu	861 vs RHE	680 vs RHE	-6.4 at 2500 rpm	3.93	0.1 M KOH	GCE	This work
Cu-N/C	No; calcinated	Cu	914 vs RHE	813 vs RHE	-5.5 at 2500 rpm	3.94	0.1 M KOH	GCE	10
Cu_3P@NPPC	No; calcinated	Cu	860 vs RHE	780 vs RHE	-6.5 at 2500 rpm	3.96	0.1 M KOH	GCE	11
Cu-N-C	No; calcinated	Cu	890 vs RHE	869 vs RHE	-5.6 at 2500 rpm	3.97	0.1 M KOH	GCE	12
Cu-N/C	No; calcinated	Cu	883 vs RHE	750 vs RHE	-5.1 at 2500 rpm	3.75	0.1 M KOH	GCE	13
Cu@Fe-N-C	No; calcinated	Cu	1010 vs RHE	892 vs RHE	-5.5 at 2500 rpm	4.00	0.1 M KOH	GCE	14
Cu-BTC	No; calcinated	Cu	-100 vs Ag/AgCl	800 vs RHE	-	3.80	0.1 M PBS (pH 6.0)	GCE	15
MOF-800	No; calcinated	Cu	-30 vs Ag/AgCl	-	-4.3 at 2500 rpm	3.98	0.05 M PBS (pH 7.0)	GCE	16
BTC-Co-O-Cu-BTA	Yes; pristine	Cu, Co	1060 vs RHE	950 vs RHE	-6.0 at 2500 rpm	3.90	0.1 M NaOH	GCE	17
CuCo@NC	No; calcinated	Cu, Co	960 vs RHE	884 vs RHE	-5.5 at 2500 rpm	3.78	0.1 M KOH	GCE	18
M-NC-CoCu	No; calcinated	Cu, Co	850 vs RHE	850 vs RHE	-4.9 at 2500 rpm	3.90	0.1 M KOH	GCE	19
Cu-MOF-74	Yes; pristine	Cu	-620 vs Ag/AgCl	-	-1.7 at 2500 rpm	4.00	0.1 M PBS (pH 7.0)	GCE	20
Cu-SAs/NSs	No; calcinated	Cu,Zn	1050 vs RHE	900 vs RHE	-5.5 at 2500 rpm	3.90	0.1 M KOH	GCE	21
Cu-CP	Yes; pristine	Cu	840 vs RHE	690 vs RHE	-3.5 at 2500 rpm	4.00	0.1 M KOH	GCE	22

VI. Performance of 2DCIFs as air electrodes in Zn-air batteries

VI.1. Description of two types of Zn-air batteries

Preparation of cathodes. To prepare the 2DCIFs-based cathodes, 25 µL of a methanolic dispersion of 2DCIFs (15 mg/mL) were drop-casted onto carbon paper or homemade carbon disks. The carbon paper used was purchased from Sigracet (BC 35) and the carbon disks were fabricated by hot pressing (at 80 °C) a mixture of carbon black and 10 % PVDF at 250 bars for 1 min. After drying under ambient temperature, the sample were coated with a drop of 5% Nafion/Isopronanol solution. On the other hand, Pt/C (60 %) was dispersed in isopropanol to obtain 15 mg/mL of Pt. Similarly, 25 µL or 50 µL of this dispersion were pipetted onto the same supports. Besides, a MnO_2-based commercial air electrode purchased from Gaskatel was used to compare the results (reference sample).

Flooded Zn-air battery. A Zn plate was used as anode and the cathode was the carbon paper-based electrodes (either modified with 2DCIFs or Pt/C). The volume of these batteries was (1 ± 0.02) mL and a 6M KOH solution was used as electrolyte. A schematic representation of the battery cell is shown in Fig. S32A.

All-solid-state Zn-air battery. A PVA-KOH gel polymer was used as electrolyte (GPE). The synthesis of these GPEs was carried out as previously reported in the bibliography.[23] In this case, 0.7 g of Zn powder (99 % from Goodfellow) was used as negative electrode and modified homemade carbon disk were the positive one. A schematic representation of the battery cell is shown in Fig. S32B.

Galvanostatic discharges at -10 mA and polarization tests were performed using a Biologic VSP potentiostat/galvanostat.

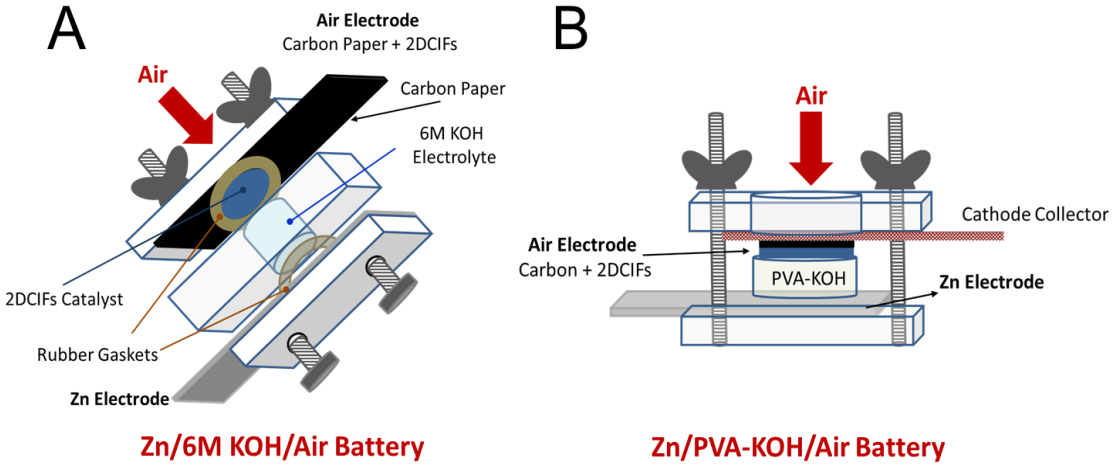

Fig. S32 Schematic representation of (A) flooded Zn/6M KOH/air battery and (B) all-solid-state Zn/PVA-KOH/air battery.

VI.2. Zn/6M KOH/air battery tests

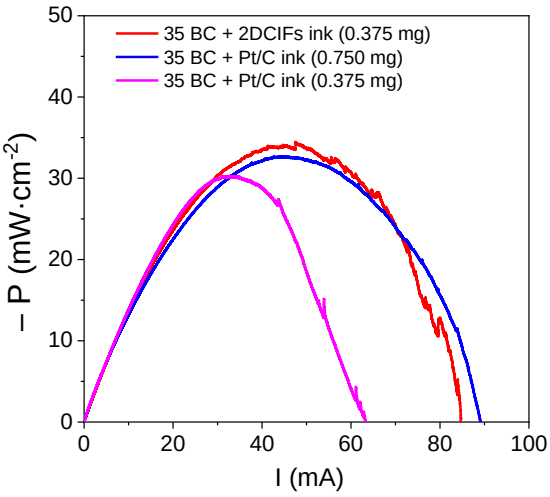

Fig. S33. Power density versus current intensity of flooded Zn/6M KOH/air batteries with different air electrodes.

VI.3. Zn/PVA-KOH/air battery tests

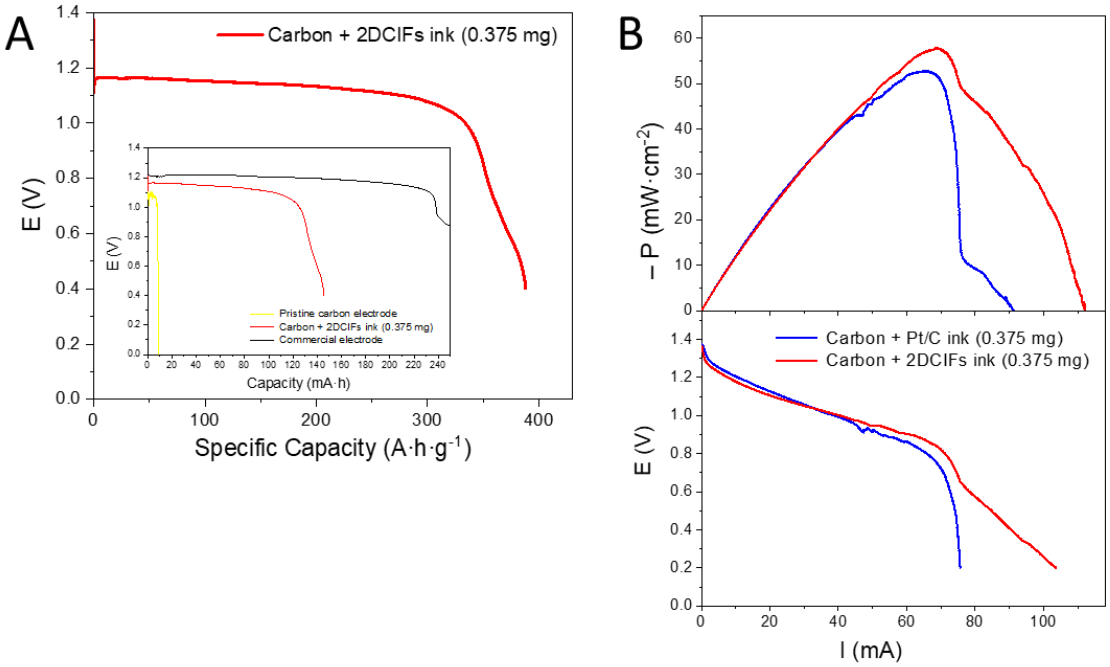

Fig. S34. (A) Galvanostatic discharges of Zn/PVA-KOH/air batteries with different air electrodes. (B) Polarization curves obtained for Zn/PVA-KOH/air batteries with 2DCIFs and Pt/C modified air electrodes (0.375 mg of 2DCIFs and Pt).

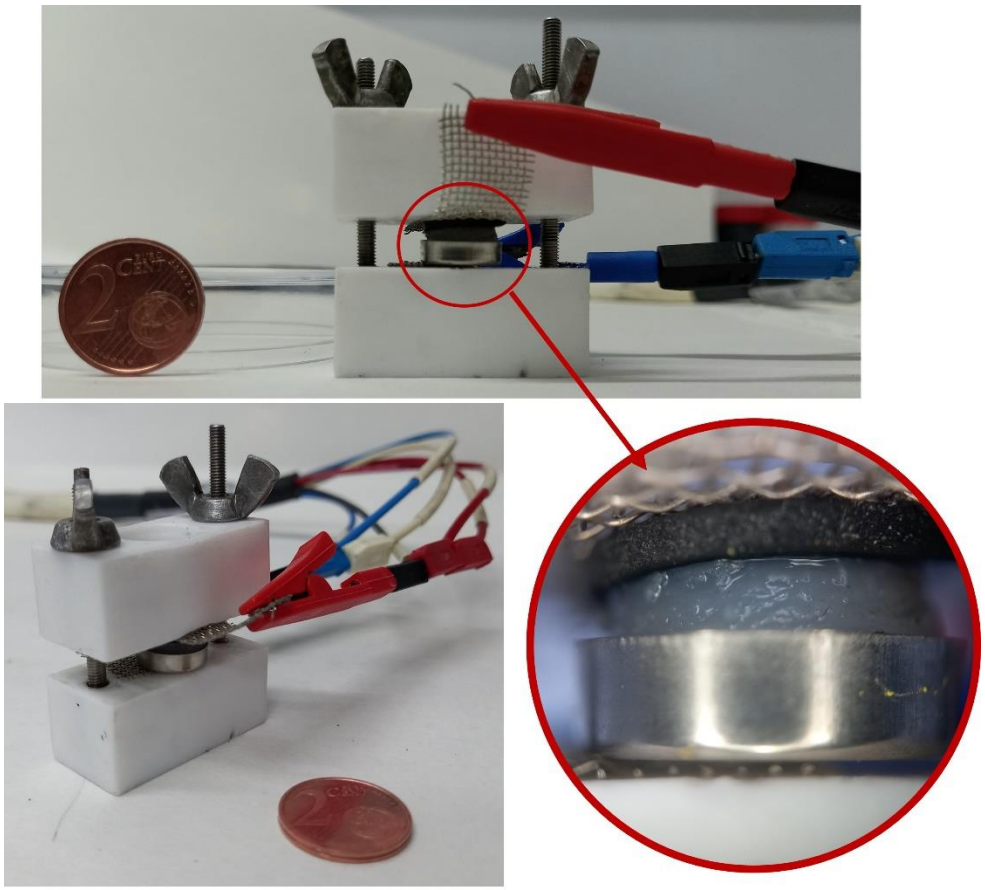

Fig. S35. Photographs of the all-solid-state Zn/PVA-KOH/Air battery used in this work.

VII. References

1. D. Alba-Molina, A. R. P. Santiago, J. J. Giner-Casares, E. Rodríguez-Castellón, M. T. Martín-Romero, L. Camacho, R. Luque and M. Cano. *J. Mater. Chem. A,* 2019, **7**, 20425-20434.
2. P. Singh and D. A. Buttry. *J. Mater. Chem. C,* 2012, **116**, 10656-10663.
3. L. Guo, J. Sun, W. Zhang, L. Hou, L. Liang, Y. Liu and C. Yuan. *ChemSusChem.* 2019, **12**, 5051-5058.
4. H. M. Rietveld, *J. Appl. Cryst*., 1969, **2**, 65-71.
5. S. Bruckner, *J. Appl. Crystallogr*., 2000, **33**, 977-979.
6. A. K. Rappe, C. J. Casewit, K. S. Colwell, W. A. Goddard and W. M. Skiff, *J. Am. Chem. Soc.,* 1992, **114**, 10024.
7. J. Luo, L. F. Ying, F. Zhang, Z. Zhou and Y. G. Zhang, *ACS omega*, 2021, **6**, 5856-5864.
8. Z. L. Ma, P. X. Liu, Z. Y. Liu, J. J. Wang, L. B. Li and L. Tian, *Inorg. Chem*., 2021, **60**, 6550-6558.
9. A. Franco, M. Cano, J. J. Giner-Casares, E. Rodríguez-Castellón, R. Luque and A. R. Puente-Santiago, *Chem. Commun.*, 2019, **55**, 4671-4674.
10. Q. Lai, J. Zhu, Y. Zhao, Y. Liang, J. He and J. Chen, *Small*, 2017, **13**, 1700740.
11. R. Wang, X. Y. Dong, J. Du, J. Y. Zhao and S. Q. Zang, *Adv. Mater.,* 2018, **30**, 1703711.
12. F. Li, G. F. Han, H. J. Noh, S. J. Kim, Y. Lu, H. Y. Jeong, Z. Fu and J. B. Baek, *Energy Environ. Sci.,* 2018, **11**, 2263-2269.
13. Q. Lai, Y. Zhao, J. Zhu, Y. Liang, J. He and J. Chen, *ChemElectroChem*, 2018, **5**, 1822-1826.
14. Z. Wang, H. Jin, T. Meng, K. Liao, W. Meng, J. Yang, D. He, Y. Xiong and S. Mu, *Adv. Funct. Mater.*, 2018, **28**, 1802596.
15. J. Mao, L. Yang, P. Yu, X. Wei and L. Mao, *Electrochem. Commun*., 2012, **19**, 29-31.
16. L. Zhang, Y. Hu, J. Chen, W. Huang, J. Cheng and Y. Chen, *J. Power Sources*, 2018, **384**, 98-106.
17. M. F. Sanad, A. R. Puente Santiago, S. A. Tolba, M. A. Ahsan, O. Fernandez-Delgado, M. Shawky Adly, E. M. Hashem, M. M. Abodouh, M. S. El-Shall, S. T. Sreenivasan, N. K. Allam and L. Echegoyen, *J. Am. Chem. Soc.,* 2021, **143**, 4064-4073.
18. M. Kuang, Q. Wang, P. Han and G. Zheng, Adv. Energy Mater., 2017, **7**, 1700193.
19. A. M. Andrade, Z. Liu, S. Grewal, A. J. Nelson, Z. Nasef, G. Diaz and M. H. Lee, *Dalton Trans.*, 2021, **50**, 5473-5482.
20. S. L. Rodríguez, M. Sánchez-Sánchez, J. M. Zamaro, J. L. Fernández, *J. Electroanal. Chem.*, 2022, **918**, 1572-6657.
21. F. Lu, K. Fan, L. Cui, Y. Yang, W. Wang, G. Zhang, C. Wang, Q. Zhang, B. Li, L. Zong, L. Wang, *Chem. Eng. J.*, 2022, **431**, 133242.
22. B. Devi, Akhil Bhardwaj, Diksha Gambhir, Biswajit Roy, Anirban Karmakar, Gourab Dey, Anuj Jain, Bhaskar Mondal, and Rik Rani Koner, *Inorg. Chem.*, 2022, **61**, 15699-15710.
23. F. Santos, J. P. Tafur, J. Abad, and A. J. Fernández Romero, *J. Electroanal. Chem*., 2019, **850**, 113380.

Annex 1

```
data_R24
_audit_creation_date              2021-10-07
_audit_creation_method            'Materials Studio'
_symmetry_space_group_name_H-M    'PC'
_symmetry_Int_Tables_number       7
_symmetry_cell_setting            monoclinic
loop_
_symmetry_equiv_pos_as_xyz
  x,y,z
  x,-y,z+1/2
_cell_length_a                    5.4340
_cell_length_b                    5.9690
_cell_length_c                    14.2531
_cell_angle_alpha                 90.0000
_cell_angle_beta                  107.1569
_cell_angle_gamma                 90.0000
loop_
_atom_site_label
_atom_site_type_symbol
_atom_site_fract_x
_atom_site_fract_y
_atom_site_fract_z
_atom_site_U_iso_or_equiv
_atom_site_adp_type
_atom_site_occupancy
Cu1    Cu    0.86714   0.46624   0.57757  19.34121  Uani   1.00
C2     C     1.37711   0.43462   0.54737   4.78617  Uani   1.00
N3     N     1.13086   0.34815   0.50978   9.36361  Uani   1.00
C4     C     1.07926   0.38384   0.41217  12.40531  Uani   1.00
C5     C     1.29276   0.48993   0.39325   8.10729  Uani   1.00
N6     N     1.48184   0.52272   0.47834   7.87167  Uani   1.00
C7     C     1.49886   0.42770   0.65183  17.09239  Uani   1.00
O8     O     1.71325   0.50128   0.70034   7.17268  Uani   1.00
H9     H     0.89579   0.33409   0.36013   2.47416  Uani   1.00
H10    H     1.31457   0.54357   0.32273   4.80944  Uani   1.00
H11    H     1.37139   0.34255   0.69059   3.08444  Uani   1.00
C12    C     1.85409   0.94785   0.53398  11.83159  Uani   1.00
N13    N     1.81785   1.11649   0.59543   9.64347  Uani   1.00
C14    C     1.98167   1.05828   0.68348  10.59048  Uani   1.00
C15    C     2.11141   0.85817   0.67338  12.74807  Uani   1.00
N16    N     2.03174   0.78720   0.57909  10.15207  Uani   1.00
C17    C     1.70703   0.95243   0.43175  10.30128  Uani   1.00
O18    O     1.71875   0.82492   0.36398  17.46014  Uani   1.00
H19    H     2.00047   1.15866   0.74943   2.61089  Uani   1.00
H20    H     2.25485   0.76479   0.72992   3.50783  Uani   1.00
H21    H     1.56440   1.09465   0.41612   2.31140  Uani   1.00
loop_
_atom_site_aniso_label
_atom_site_aniso_U_11
_atom_site_aniso_U_22
_atom_site_aniso_U_33
_atom_site_aniso_U_12
_atom_site_aniso_U_13
_atom_site_aniso_U_23
```

```
Cu1      22.84338  20.71042  22.07806 -19.66007  18.39927 -18.58317
C2        3.13104  10.44299   0.80638   0.77255   0.61462   1.53945
N3       21.81110   2.66929   8.45164   0.23741  11.95528  -0.98039
C4        3.89045   8.31739  27.04279   4.51518   7.71116  12.36365
C5        4.29328  18.60372   0.91055   7.16799  -0.02837  -1.98632
N6        7.80305   3.13719  10.45840   1.59234  -0.73633   1.58472
C7        3.71256   1.65914  44.49282   1.11078   4.92398  -0.59541
O8        5.88719  14.57570   1.08821   0.77201   1.08001   3.37778
H9        5.43136   0.22845   1.14593  -0.02342   0.01574  -0.46761
H10       7.01550   4.71335   3.49826  -2.32245   2.78684   1.44462
H11       2.29429   6.21547   1.51212  -1.93747   1.75075  -1.56847
C12      15.46784  10.57493  12.78275  -9.47970   9.32107  -7.00291
N13      24.59187   1.92421   7.18683   4.07670  12.07258   3.05060
C14       3.24200  16.68877  10.38609  -0.44014  -0.24084   8.98883
C15      22.05415   0.47530  11.14315  -0.41516  -2.17806   0.78583
N16       5.47638  10.22193  15.36881   4.04312   4.01991  10.16860
C17      13.18461   8.68183   4.72508  -2.70344  -4.03165   1.22139
O18       3.23680   6.95166  32.73268   2.75232  -9.33277  -5.52120
H19       0.14709   3.66117   3.76287  -0.59563   0.17195  -0.39306
H20       2.44359   3.80783   4.86653   1.28027   1.99810   3.83186
H21       0.71968   5.23083   1.18680  -0.61633   0.59552   1.10064
loop_
_geom_bond_atom_site_label_1
_geom_bond_atom_site_label_2
_geom_bond_distance
_geom_bond_site_symmetry_2
_ccdc_geom_bond_type
C2     N3      1.386   .     A
C2     N6      1.378   .     A
C2     C7      1.441   .     S
N3     C4      1.352   .     A
C4     C5      1.416   .     A
C4     H9      1.094   .     S
C5     N6      1.353   .     A
C5     H10     1.094   .     S
C7     O8      1.246   .     D
C7     H11     1.126   .     S
C12    N13     1.386   .     A
C12    N16     1.378   .     A
C12    C17     1.441   .     S
N13    C14     1.352   .     A
C14    C15     1.416   .     A
C14    H19     1.094   .     S
C15    N16     1.353   .     A
C15    H20     1.094   .     S
C17    O18     1.246   .     D
C17    H21     1.126   .     S
```